Supporting Information for

Design of SrTiO₃-Based Catalysts for Photocatalytic CO₂ Reduction

Bíborka Boga[1,2], Nikolaos G. Moustakas[1], Yunyan Han[1,3], Haijun Jiao[1], Carsten Kreyenschulte[1], Pawel Naliwajko[1], Thi Thanh Hoa Duong[1], Shuoping Ding[1], Anh Binh Ngo[1], Abdo Hezam[4], Tim Peppel[1], Vasile-Mircea Cristea[2], Norbert Steinfeldt[1]*, Jennifer Strunk[1,4]*

[1]*Leibniz Institute for Catalysis e.V. (LIKAT), Albert Einstein St., 29.A, Rostock, 18059, Germany*

[2]*Faculty of Chemistry and Chemical Engineering, Babes-Bolyai University, Arany Janos St, 11, Cluj-Napoca, 400028, Romania*

[3]*Shaanxi Key Laboratory of Phytochemistry, College of Chemistry & Chemical Engineering, Baoji University of Arts and Sciences, Baoji 721013, China*

[4]*Industrielle Chemie und Heterogene Katalyse, Technical University of Munich (TUM), Lichtenberg St, 4, Munich, 85745, Germany*

Correspondings authors: Norbert.Steinfeldt@catalysis.de, Jennifer.Strunk@tum.de

Content

Section 1: ICP Results

Table S1. The Au and Ni^{2+} content of the studied samples

No.	Sample	Au_{exp} (wt%)	Au_{theo} (wt%)	Ni^{2+}_{exp} (wt%)	Ni^{2+}_{theo} (wt%)
1	NiO/STO-SCO (HT)	--	--	0.31	0.30
2	Au-STO-SCO (HT)	0.90	1.00	--	--
3	Au-NiO/STO-SCO (HT)	0.78	1.00	0.31	0.30
4	NiO/STO	--	--	0.27	0.30
5	Au-STO	0.91	1.00	--	--

*Abbreviations in Table S1: exp – experimental, theo – theoretical.
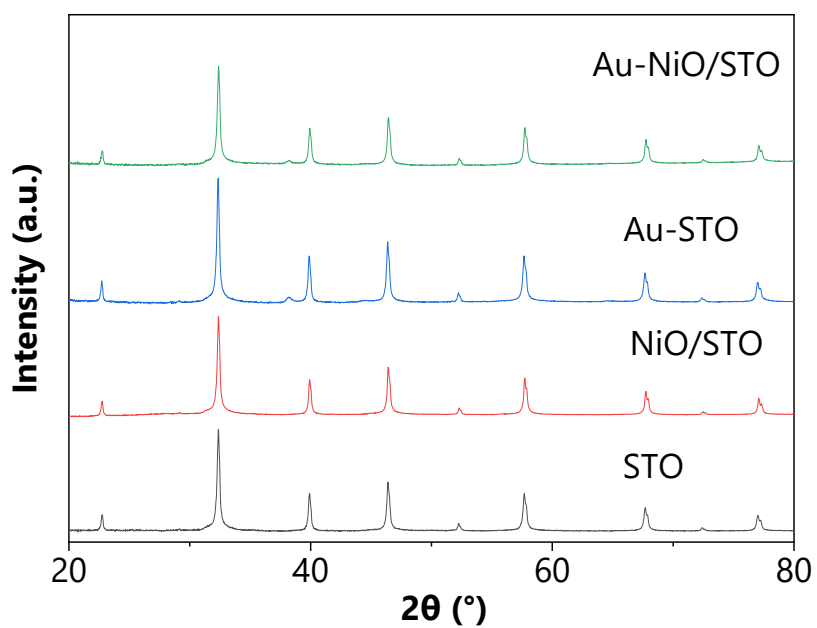
Section 2: XRD Results

Figure S1. XRD patterns of the STO-based catalysts in 20-80 2θ (°).
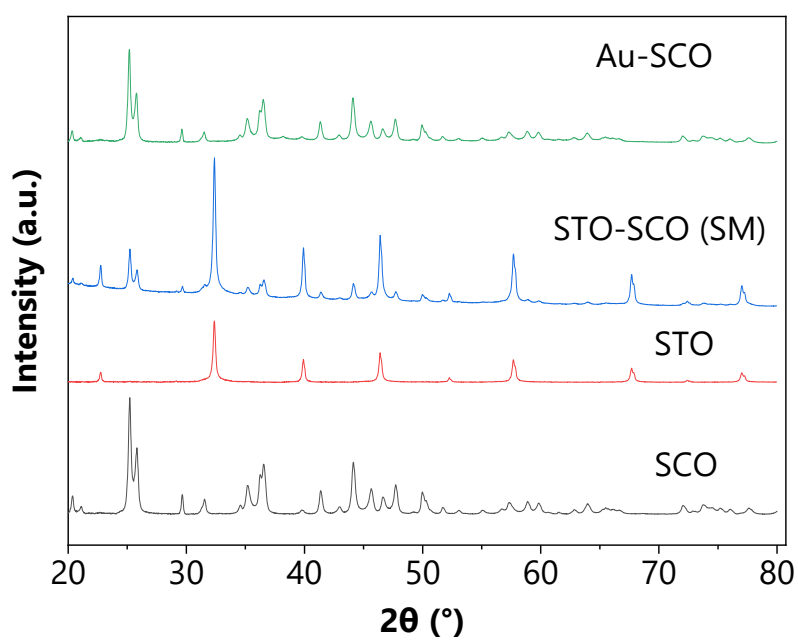

Figure S2. XRD patterns of the commercial catalysts (STO and SCO), STO-SCO (SM), and Au-SCO, respectively.

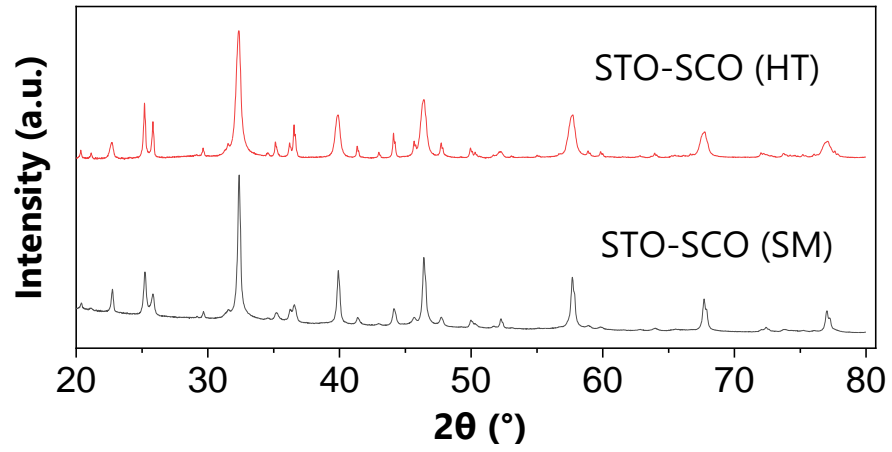**Figure S3**. Comparison between the XRD patterns of STO-SCO (HT) and STO-SCO (SM) in 20-80 2θ (°).

Section 3: XPS results

Table S2. Selected descriptors in association with their binding energy from Au-STO-SCO (HT) and Au-NiO/STO-SCO (HT)

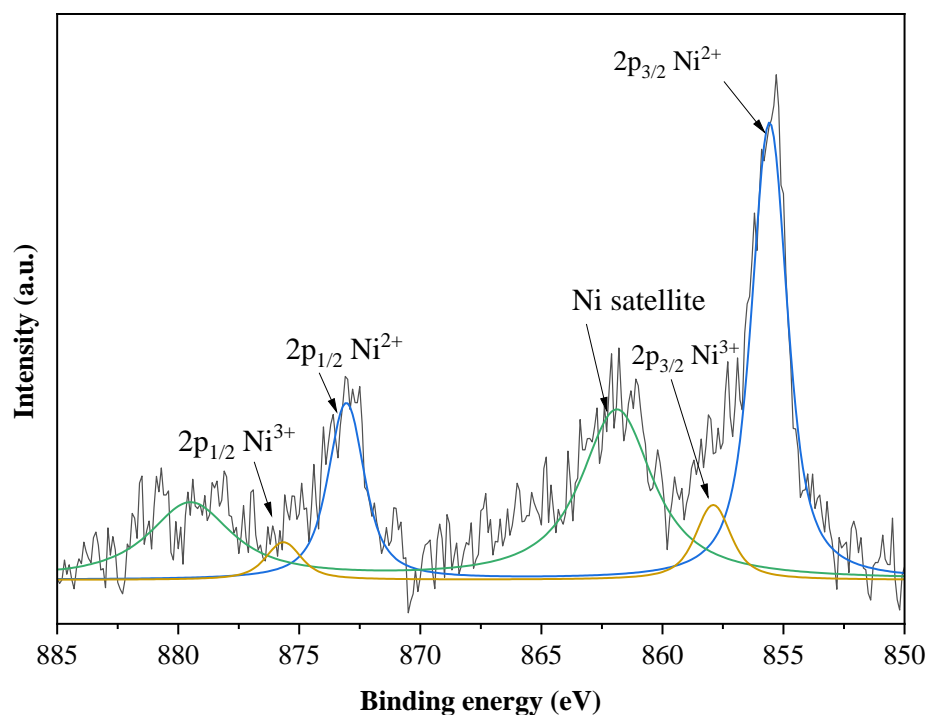| Descriptors	Binding energy (eV)	
	Au-STO-SCO (HT)	**Au-NiO/STO-SCO (HT)**
Sr3d doublet 1	132.82	132.89
Sr3d doublet 2	133.79	133.85
Ti2p doublet 1	458.24	458.31
Ti2p doublet 2	471.71	471.83

Figure S4. Ni 2p XP spectra in Au-NiO/STO-SCO (HT) (The assignment has been done considering the references [1,2]).
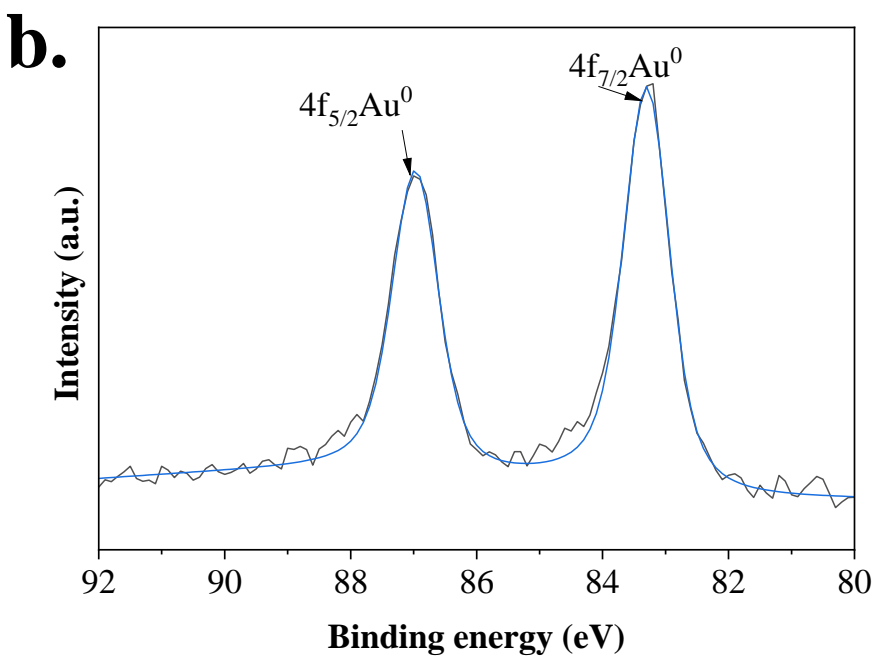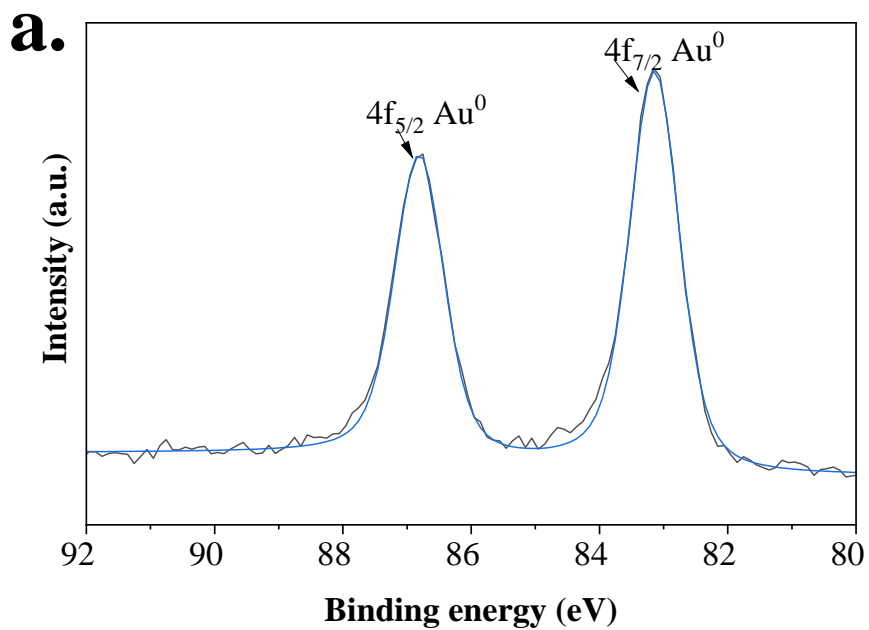
Figure S5. a. Au 4f XP spectra in Au-STO-SCO (HT). b. Au 4f XP spectra in Au-NiO/STO-SCO (HT) (Assignment performed considering ref. [3]).

Table S3. Experimental (XPS-based) and theoretical composition of the species in case of Au-STO-SCO (HT)

Species Au-STO-SCO (HT)	Experimental atomic composition (at %)	Theoretical atomic composition in the bulk (mol %)
Au	0.34	0.15
Sr	16.59	15.99
Ti	16.39	16.40
C	13.8	3.01
O	52.2	64.46

Table S4. Experimental (XPS-based) and theoretical composition of the species in case of Au-NiO/STO-SCO (HT)

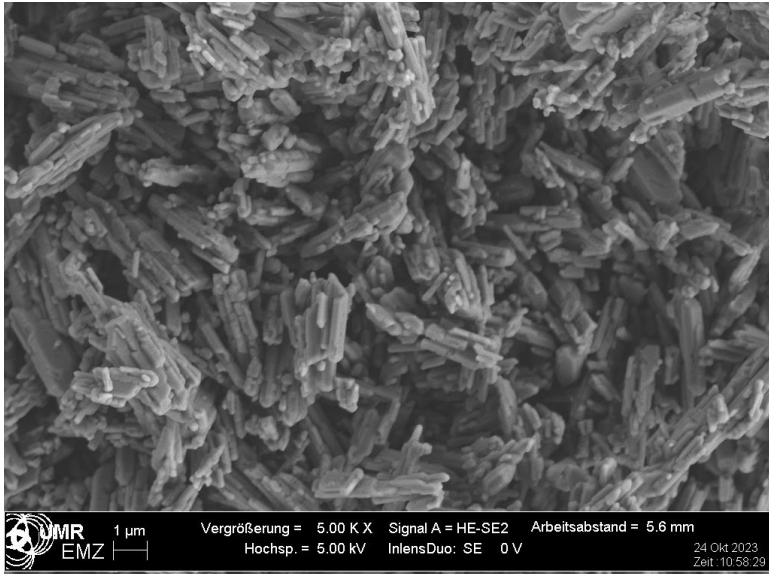| Species Au-NiO/STO-SCO (HT)	Experimental atomic composition (at %)	Theoretical atomic composition in the bulk (mol %)
Au	0.29	0.14
Ni	0.52	0.18
Sr	16.73	17.75
Ti	16.09	18.42
C	14.17	3.19
O	51.66	60.31

Section 4: SEM

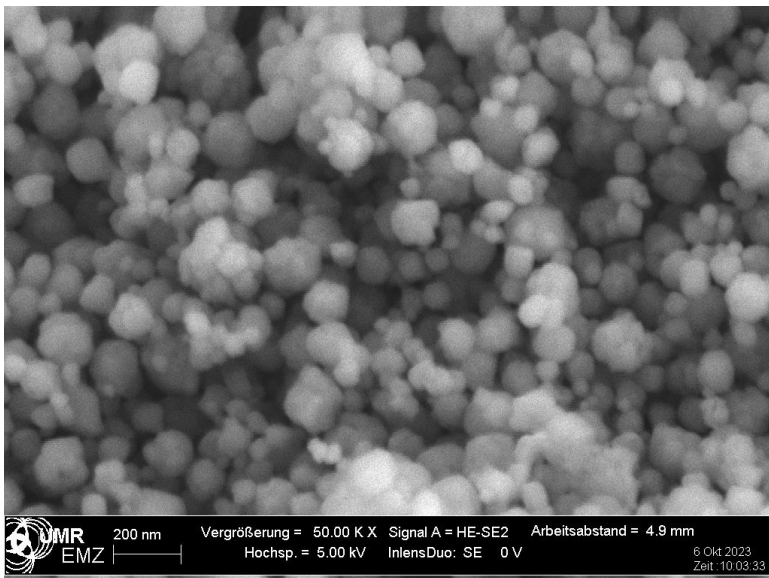**Figure S6**. SEM image of SCO (Meck).

Figure S7. SEM image of STO (Iolitec).
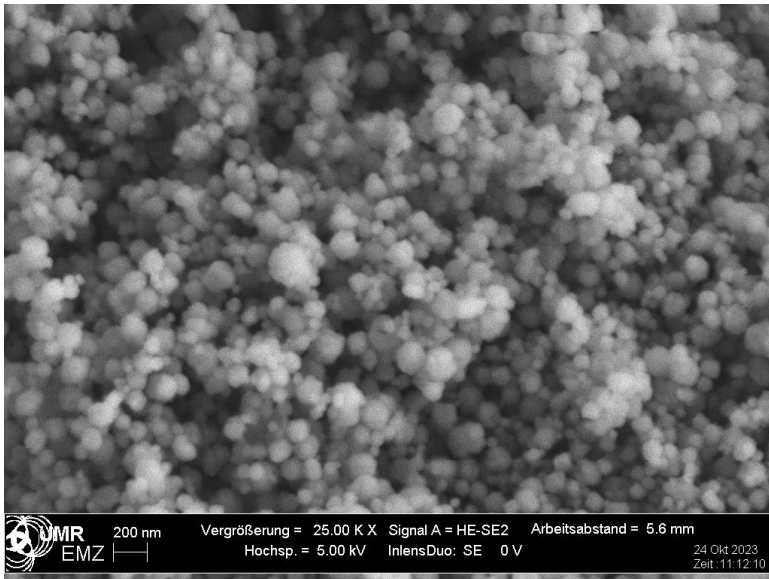
Figure S8. SEM image of NiO/STO.
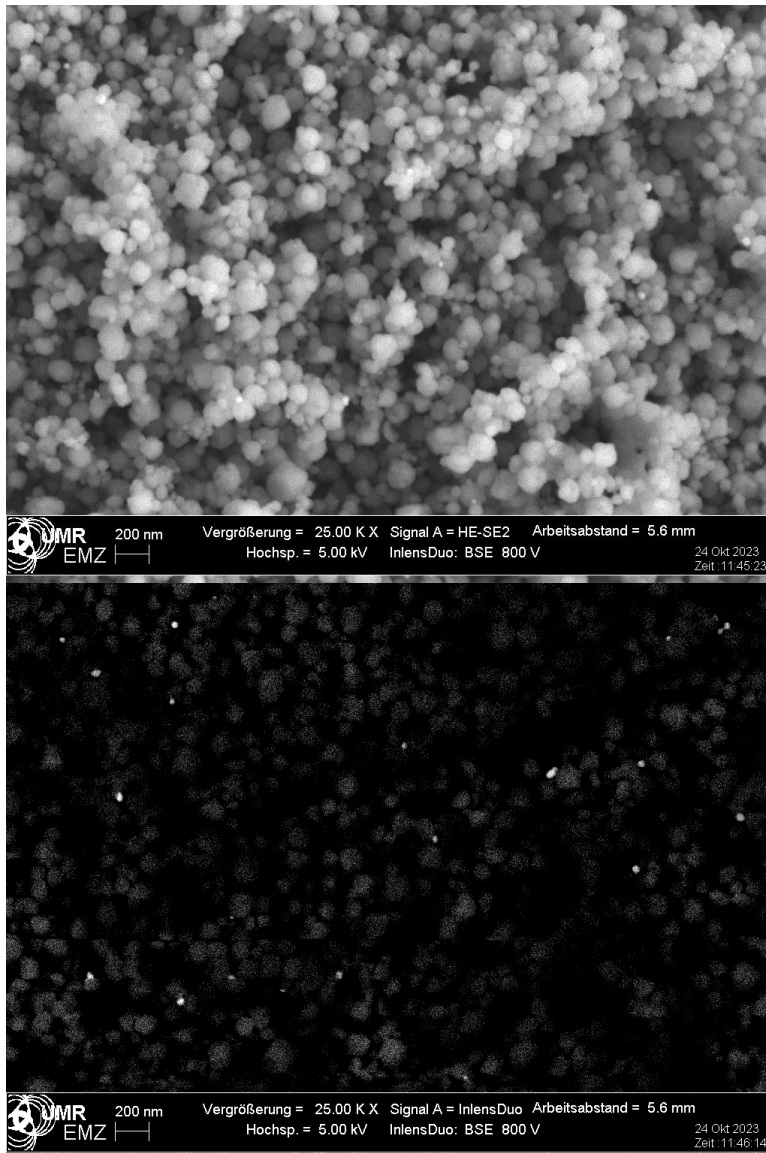
Figure S9. SEM image of Au-STO.
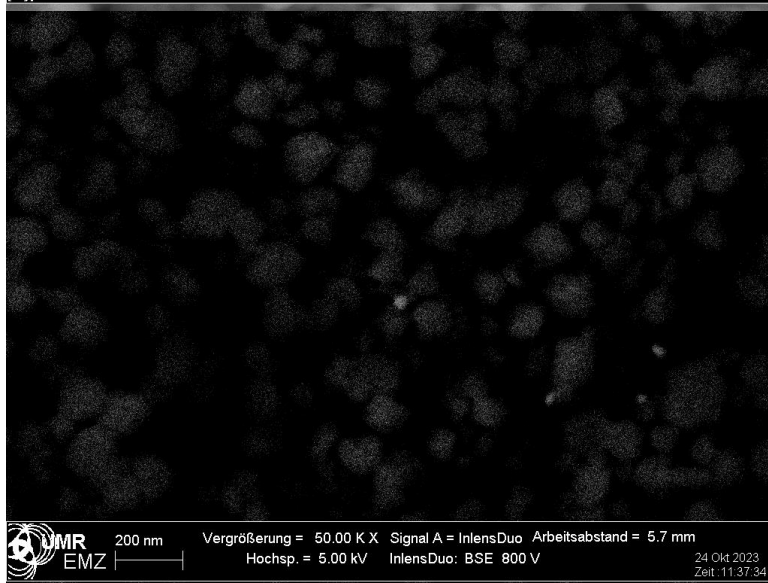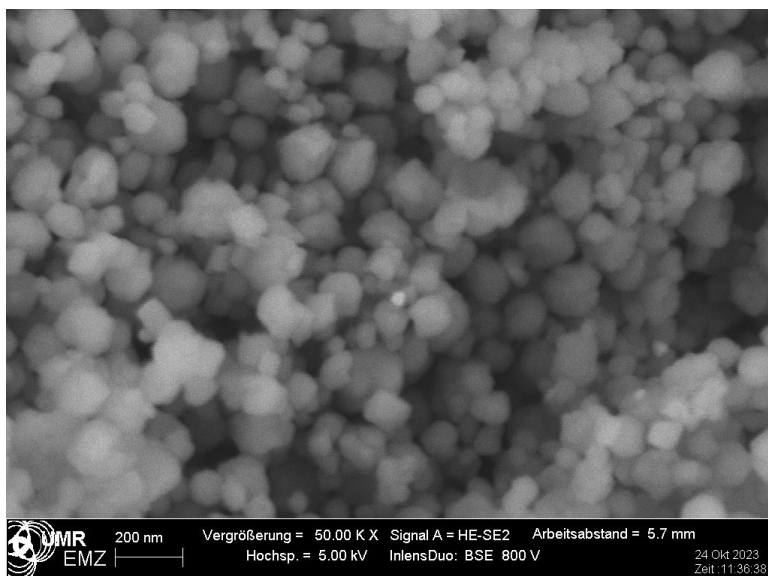
Figure S10. SEM image of Au-NiO/STO.
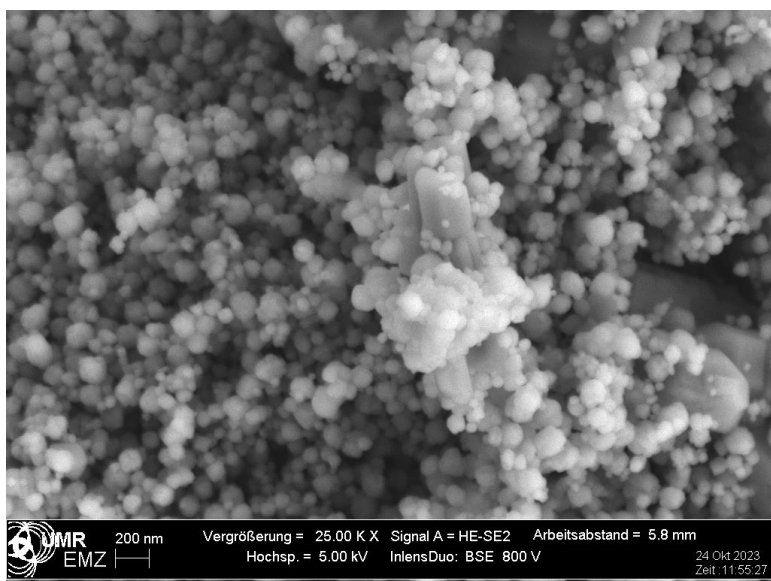
Figure S11. SEM image of STO-SCO (SM).
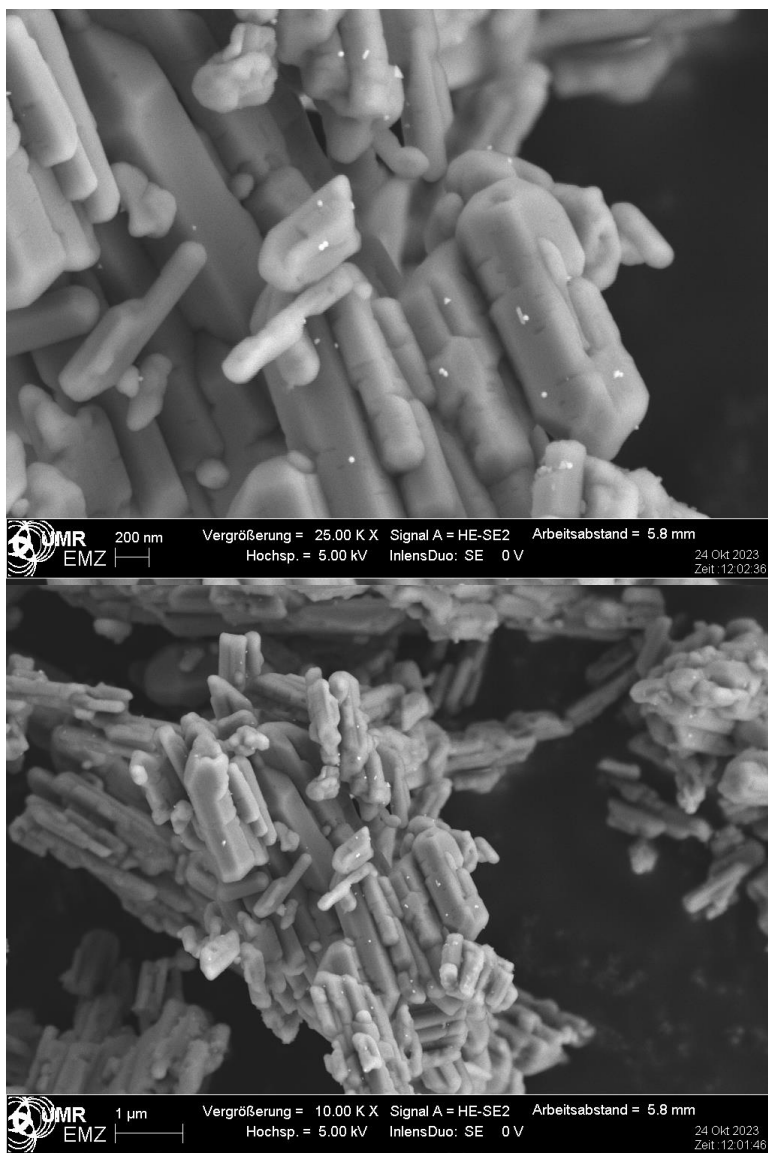
Figure S12. SEM image of Au-SCO.

Section 5: STEM
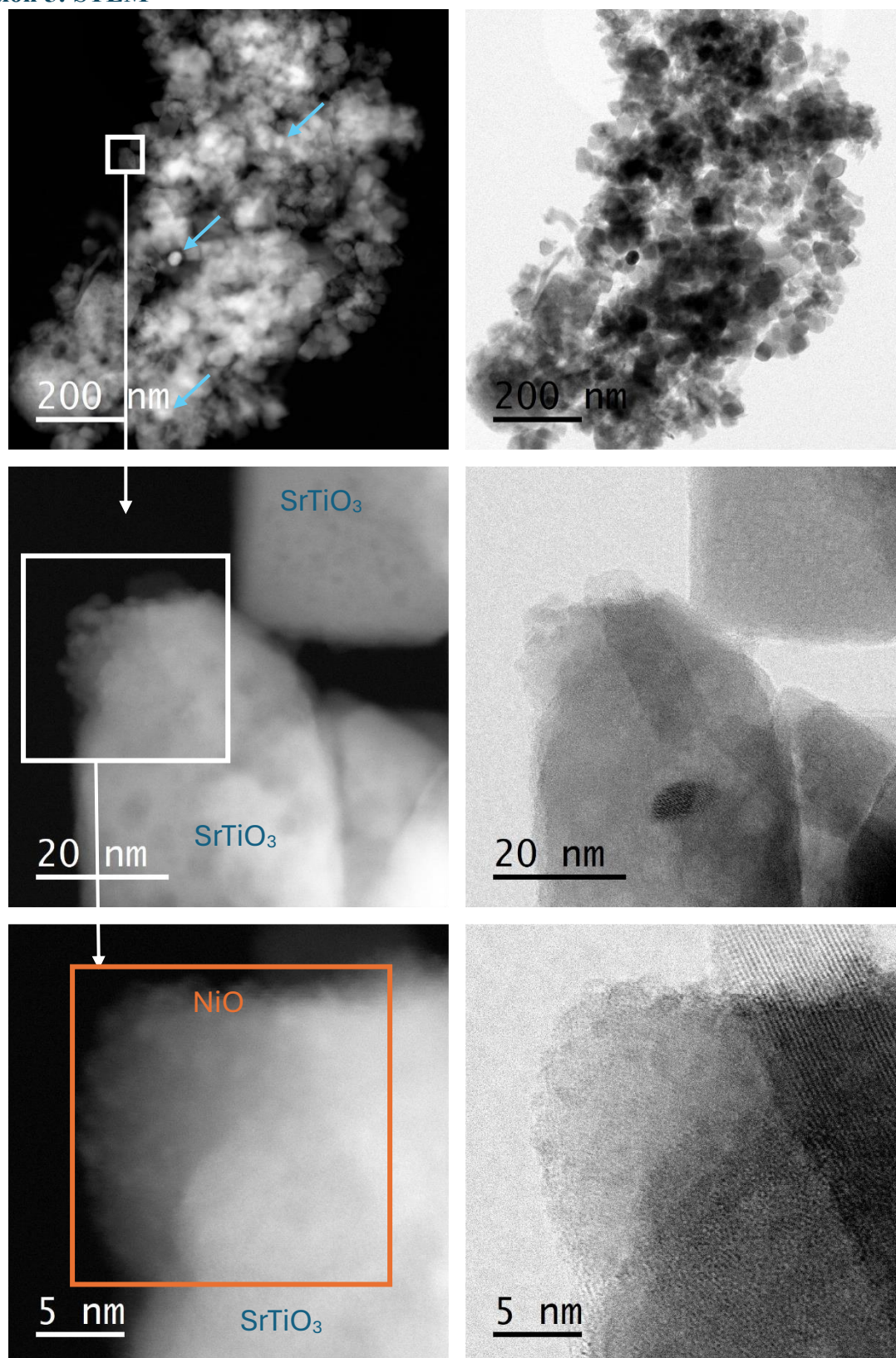
Figure S13. HAADF-STEM images (left column) and corresponding ABF-STEM images (right column) of Au-NiO/STO-SCO (HT) showing a magnification series of a NiO particle (marked by orange frame) adhering to a SrTiO₃ (blue) particle surface. Gold particles have been marked in yellow.
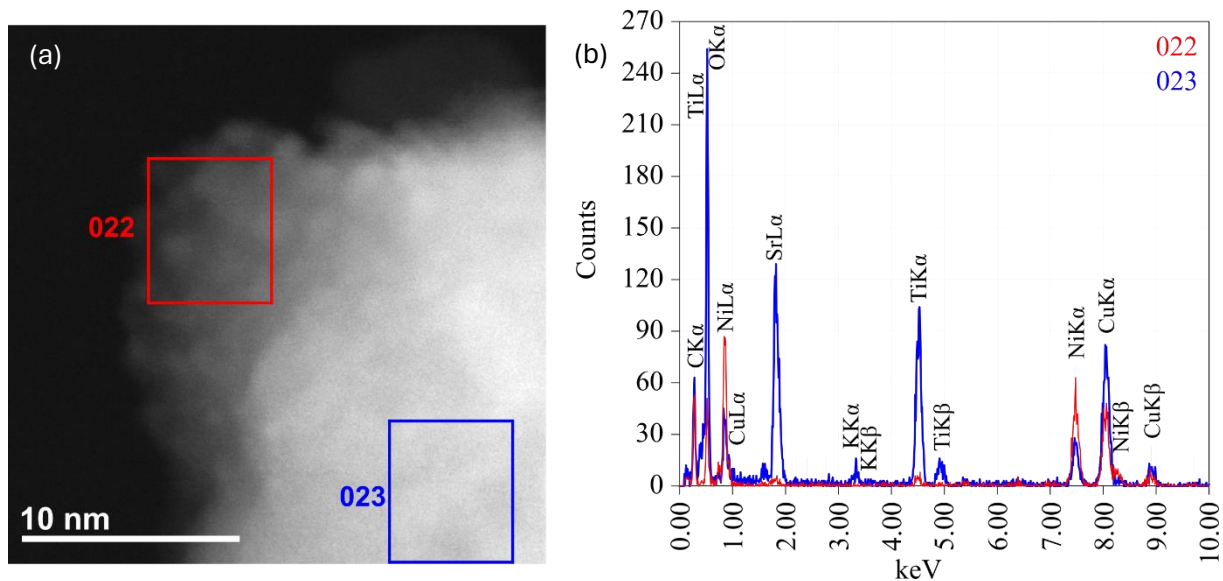
Figure S14. HAADF-STEM image (a) of Au-NiO/STO-SCO (HT) and EDX spectra (b) from marked regions in (a) showing the presence of Ni and O in region 022 whereas Sr and Ti are not present there. The spectra have been scaled to matching Cu-Kβ intensities for better visual clarity.
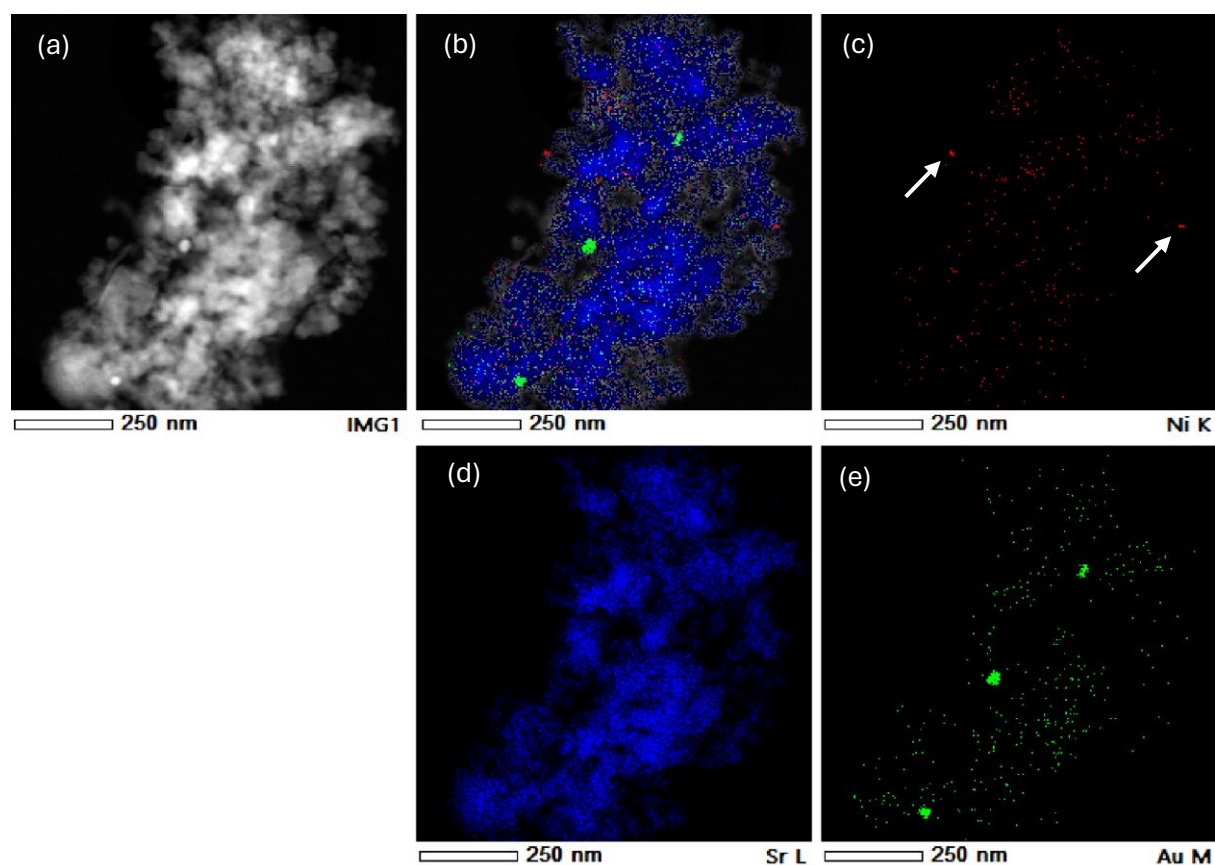
Figure S15. HAADF-STEM image of Au-NiO/STO-SCO (HT) (a), HAADF images overlaid with elemental maps (b) and the single elemental maps of Ni (c), Sr (d), and Au (e). The two assumed NiO particles are marked by arrow, as they are barely noticeable due to low x-ray count numbers.
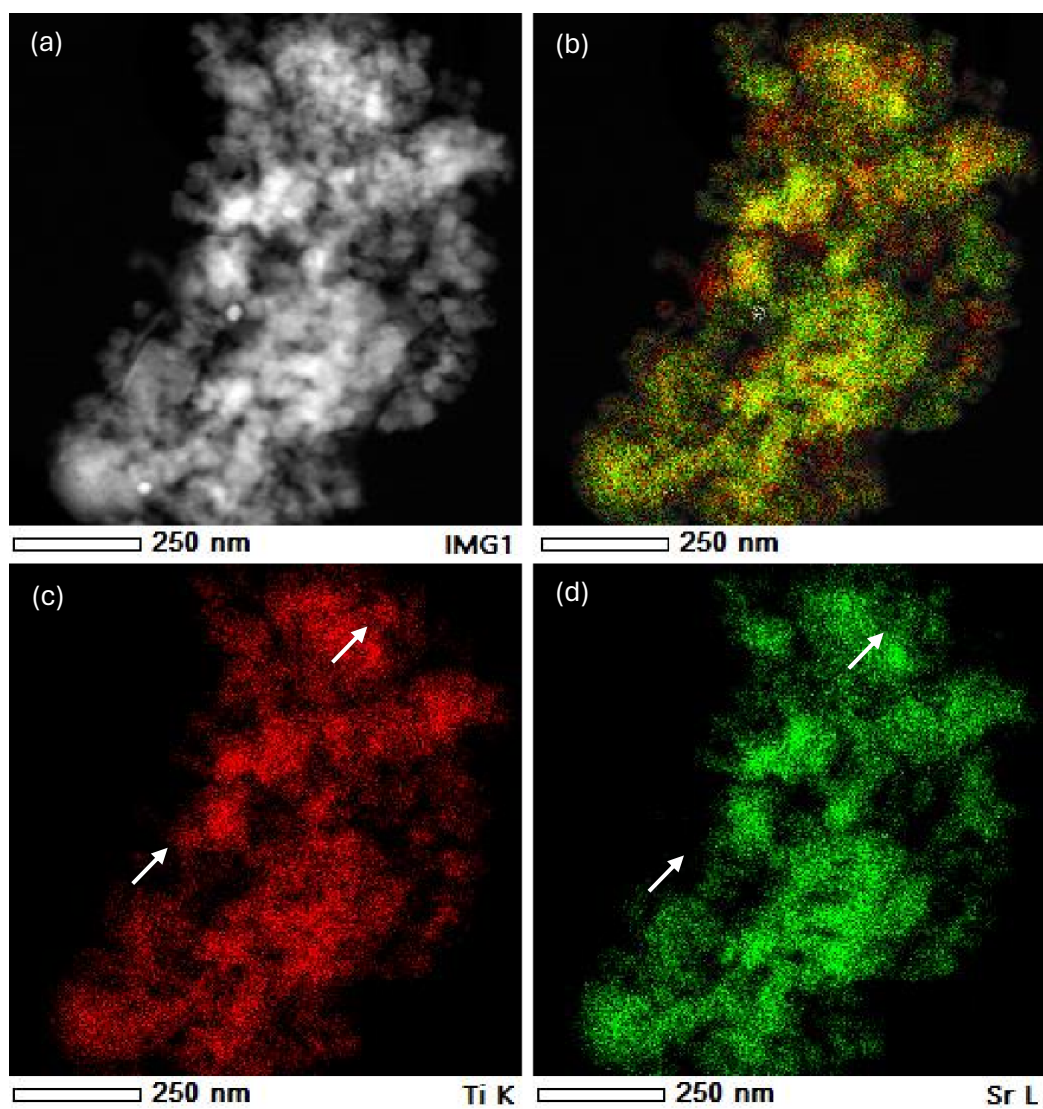
Figure S16. HAADF-STEM image of Au-NiO/STO-SCO (HT) (a), HAADF images overlaid with elemental maps (b) and the single elemental maps of Ti (c), and Sr (d). Differences (arrow) in Ti and Sr maps indicate local variations of composition.
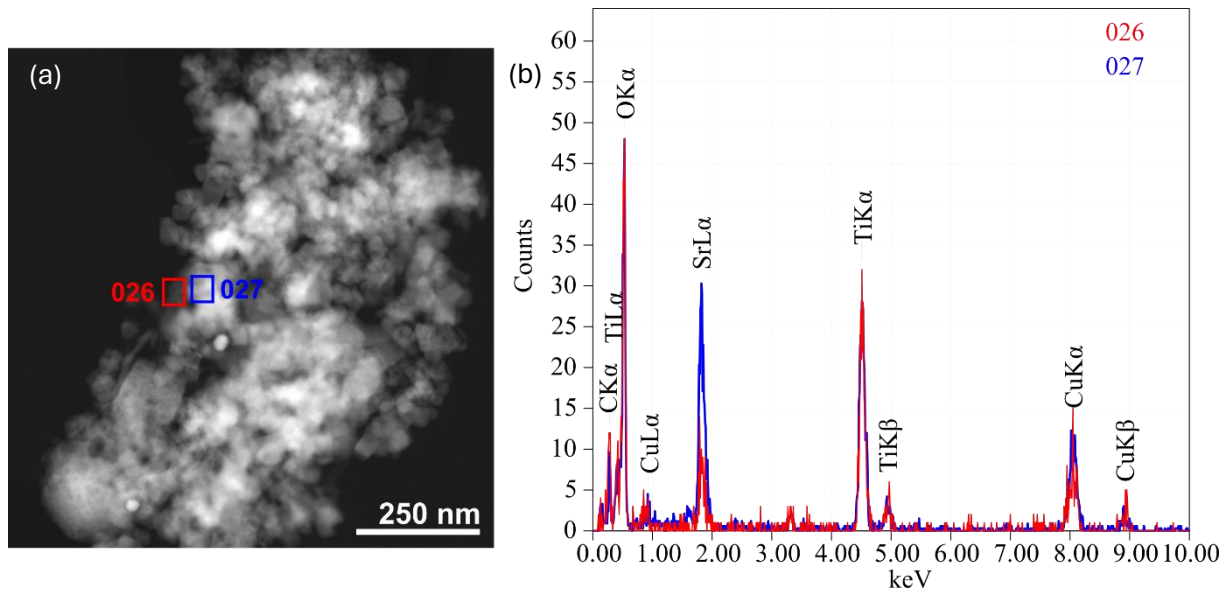
Figure S17. HAADF-STEM image (a) of Au-NiO/STO-SCO (HT) and EDX spectra (b) from marked regions in (a) showing the compositional variation in the ratio of Ti and Sr.
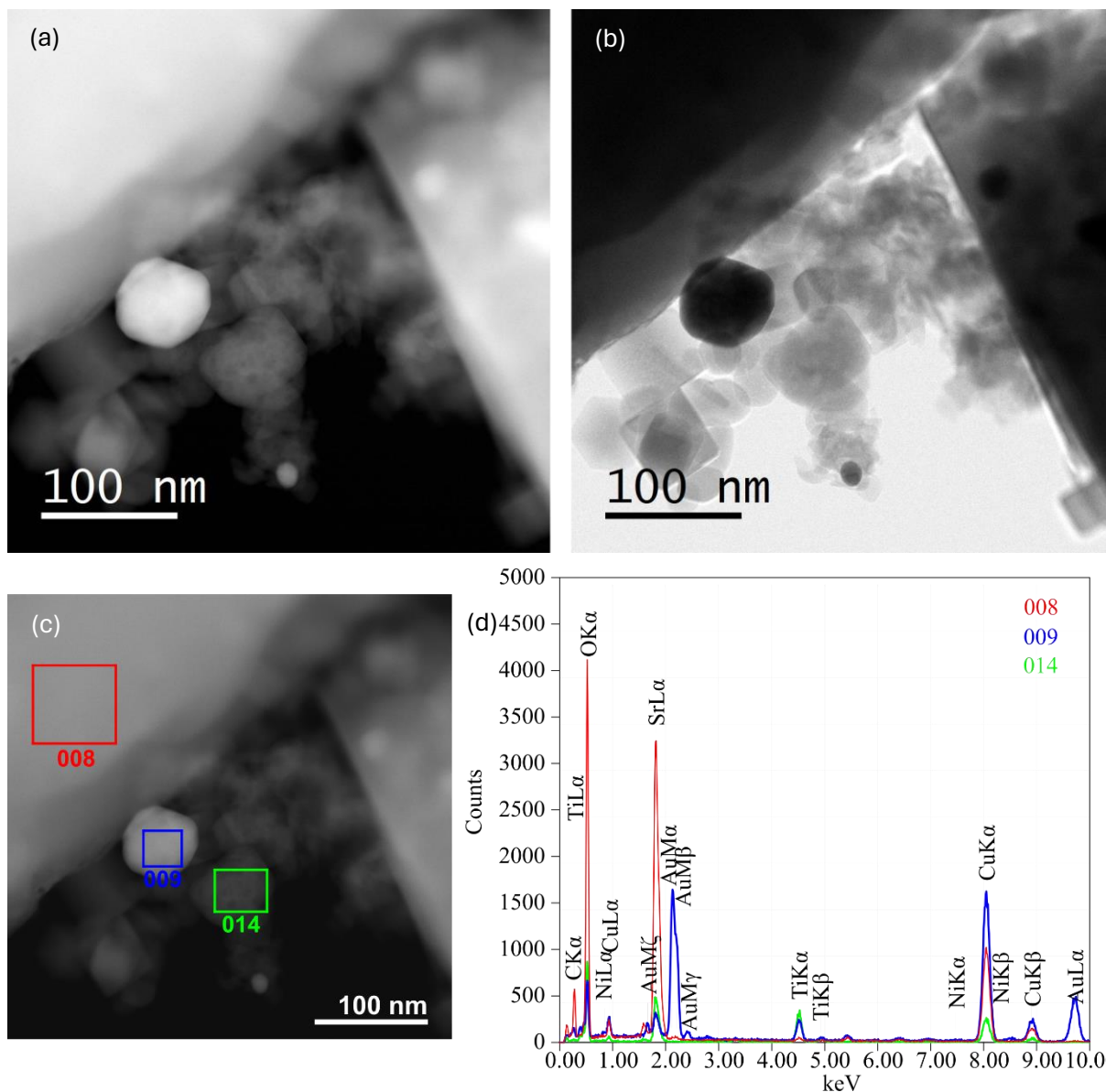
Figure S18. HAADF-STEM images (a, c), ABF-STEM image (b) of Au-NiO/STO-SCO (HT), and EDX spectra (b) from marked regions in (c) providing the assignment of the smaller grains to be $SrTiO_3$ (green), the more intense particles (blue) to be Au and the large particle to be $SrCO_3$ (red).

Section 6: Textural properties of the samples
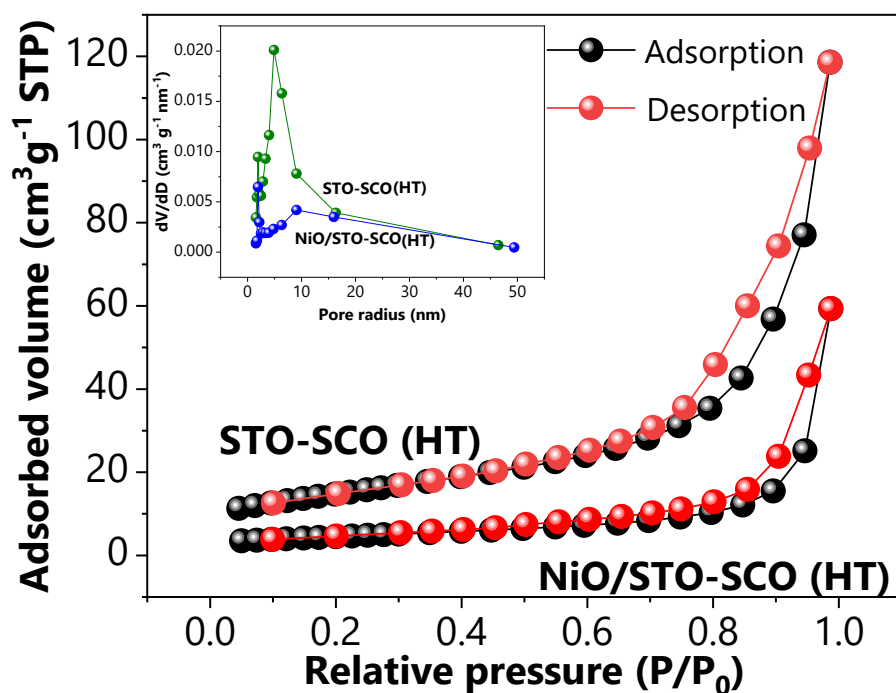
Figure S19. Nitrogen adsorption/desorption isotherms in association with the pore size distribution (inset) in case of the STO-SCO (HT) and NiO/STO-SCO (HT) supports.
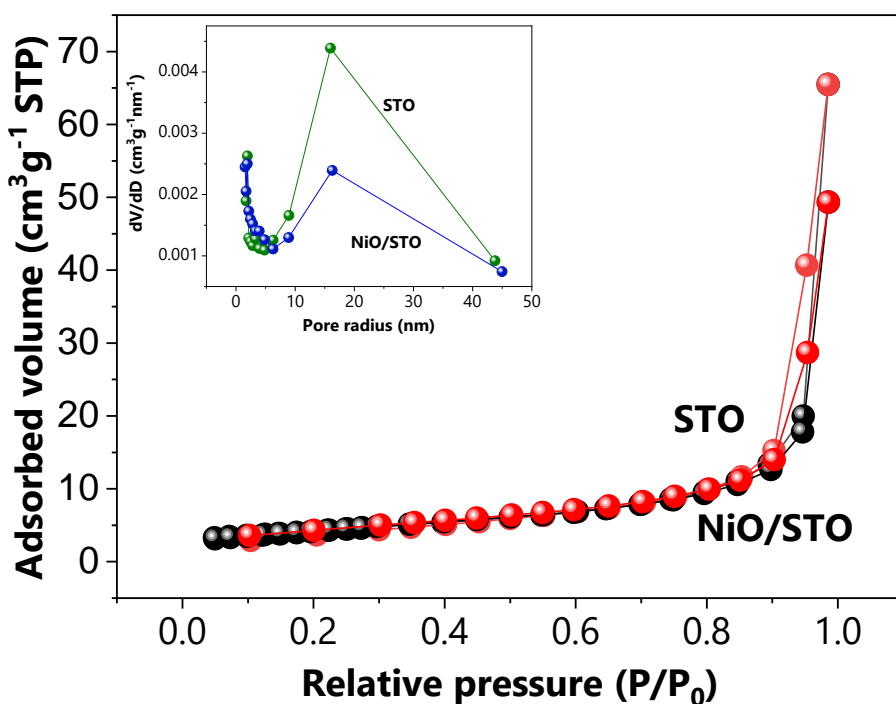
Figure S20. Nitrogen adsorption/desorption isotherms in association with the pore size distribution (inset) in case of the STO and NiO/STO supports.

Section 7: Optical properties of the samples
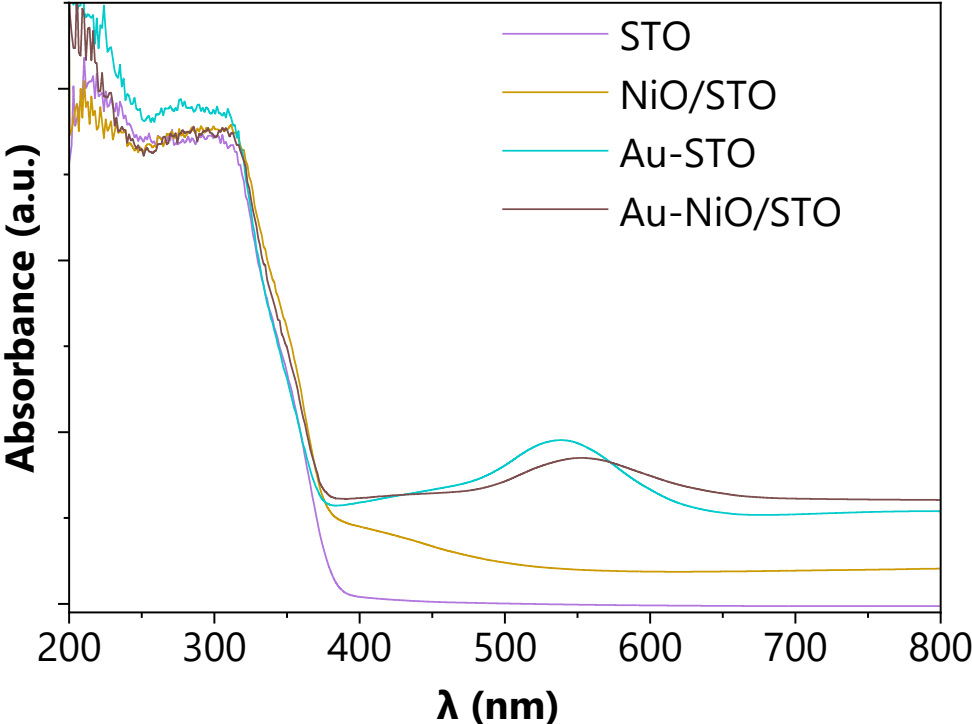
Figure S21. The UV-Vis spectra of the reference sample series.

Section 8: *In situ* EPR
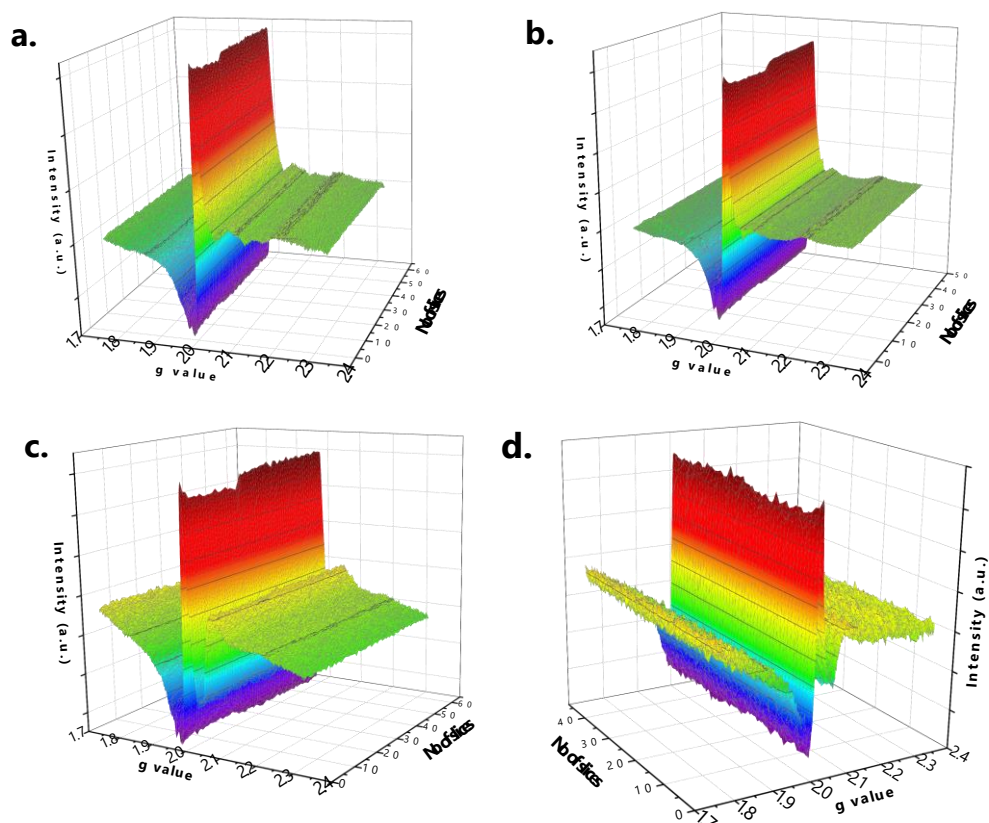
Figure S22. Serial *In situ* EPR measurements (a. STO-SCO (HT), b. NiO/STO-SCO (HT), c. Au-STO-SCO (HT), d. Au-NiO/STO-SCO (HT)).

Table S5. Comparative analysis of the literature data and the identified species in association with the g values in the EPR spectra

Species	Signal	Ref 1	Ref 2	Ref 3	Ref 4	Our work
OV trapped e^-	Isotropic	$g_1=g_2=g_3=2.003$ [4]	2.005 [5]	2.004 [6]	2.004 [7]	2.004
Ti^{3+}	Anisotropic	$g_1=1.975$ $g_2=1.975$ $g_3=1.951$ $(Ti^{3+}$ rutile) [5, 8]	--	--	--	1.978

Section 9: *In situ* DRIFTS

During the DRIFTS interpretation the following principles were applied: (i) the assignment was done considering the simultaneous change of the vibrational features, (ii) both raw and difference spectra were considered. At the same it worths to mention that the previous principle regarding to the simultaneous assignment was not always possible since some groups may not feature symmetrical and asymmetrical band due to the selection rules, or one band may be covered by another band.

STO-SCO (HT), NiO/STO-SCO (HT), Au-STO-SCO (HT). According to Figure S23- S28 and Table S6, carboxylates [9], and monodentate bicarbonates [10] were identified in the DRIFT spectra collected while using STO-SCO (HT), NiO/STO-SCO (HT) or Au-STO-SCO (HT). Additionally, in the spectra of Au-STO-SCO (HT) the band at 1311 cm^{-1} can be attributed to bidentate carbonates [10]. While the disturbance signal can be observed at 1410 cm^{-1} for NiO/STO-SCO (HT) (Figure S26), in the case of STO-SCO (HT) (Figure S24) it can be identified at 1575 cm^{-1}, which can be assigned to the interference of IR beam with the visible light, even though the visible irradiation was performed at a very lowest intensity.

Table S6. Systematic approach for the assignment of vibrational bands (by specifying the wavenumbers, at cm^{-1}) in the dark

Species	Au-NiO/STO-SCO (HT)	Au-STO-SCO (HT)	NiO/STO-SCO (HT)	STO-SCO (HT)
Linearly adsorbed CO_2	1270 [10]	--	1281 [10]	1281 [10]
Monodentate carbonate	1586 [10]	--	1582 [10]	1582 [10]
Monodentate bicarbonates	1221 +1624 [10]	1221 +1624 [10]	1221+1687 [10]	1221+1682 [10]
Bidentate carbonate	--	1311 [10]	--	--
Carboxylates	1350 +1624 [9]	1350+1624 [9]	1334+1644 [9]	1334+1646 [9]

Au-NiO/STO-SCO (HT). The group of features at 1221 cm^{-1} were identified not only in the DRIFT spectra of Au-NiO/STO-SCO (Figure 5, Table S7), but in all DRIFT spectra (Figures S23 – S28), which can be assigned to the bending vibrational mode of COH (δ(COH)) from mono- and bidentate bicarbonate species [10]. Considering its relatively low stability (instantaneous desorption when no CO_2 is present), it is highly probable that this feature is

associated with a monodentate bicarbonate species in our case. Interestingly in the case of both Au-STO-SCO (HT) and Au-NiO/STO-SCO (HT), considerable decrease in the intensity of the feature at 1221 cm^{-1} was observed under irradiation by light in the visible range (500-700 nm) (in comparison to the irradiation via λ: 320-500 nm), which may indicate the visible light activity of Au-NiO/STO-SCO (HT), and implicitly the modification of the mechanism under visible irradiation.

Furthermore, the features at 1624 and 1350 cm^{-1} can be ascribed to the asymmetrical OCO (ν_{as}(OCO)) and symmetrical CO stretching vibration (ν_s(CO)) of the surface carboxylates [9] in the case of Au-NiO/STO-SCO (HT) (Figure 5) and Au-STO-SCO (HT) (Figure S27 – S28). On the other hand, the feature 1624 cm^{-1} may also be assigned to the asymmetric CO stretching from strongly bound bidentate bicarbonates (ν_{as}(CO)) [11], however considering the previous reasoning related to the instantaneous disappearance of the band 1221 cm^{-1} in the absence of CO_2 (which indicated the formation of monodentate bicarbonates), the assignment related to the formation of (stable) bidentate bicarbonate has not been further supported.

Finally, while the feature at 1586 cm^{-1} can be assigned to the asymmetric OCO stretching mode (ν_{as}(OCO)) [12] from bidentate carbonates, the relatively low intensity feature at 1270 cm^{-1} designates the linearly adsorbed CO_2 in the DRIFT spectra related to Au-NiO/STO-SCO (HT) (Figure 5).

Under irradiation negative bands were identified at 1435, 1400 and 1390 cm^{-1} in the case of all studied samples (Figures S24, S26, S28), which can be directly assigned to the structural carbonates or spectator carbonate species present in the beginning of the measurement. Moreover, in the case of Au-NiO/STO-SCO (HT) two additional negative features were identified, at 1550 and 1515 cm^{-1} (Figure 5). These structural carbonates or spectator carbonate species can participate in the formation of (presumably) structurally very different species. These newly formed species can be identified only in the presence of CO_2, and they completely disappear when CO_2 is removed. The potential assignment of the previously mentioned features is the following: ν_{as}(OCO) at 1550 cm^{-1} [13], ν_s(OCO) at 1390 and 1435 cm^{-1} [9, 13-17] from bicarbonate species, respectively ν_{as}(OCO) at 1515 cm^{-1} [11], ν_s(CO_3) at 1435 [13], ν_s(OCO) at 1400 cm^{-1} [11] from monodentate carbonate.

It should be highlighted, that under visible light irradiation (400-700 nm) the only observable signals can be identified at 1414 and 1560 cm^{-1} in Table S9. These can be associated with the characteristic vibrational modes, i.e., ν_{as}(COH) at 1414 cm^{-1} [10, 18]; ν_{as}(OCO) [11] at 1560 cm^{-1} [19], of bidentate carbonates. Furthermore, the previously formed bicarbonates (i.e., at 1221

and 1624 cm^{-1}, under λ= 320-400 nm) cannot be identified in the spectra recorded under λ=400-700 nm, which indicates their visible light-induced transformation.

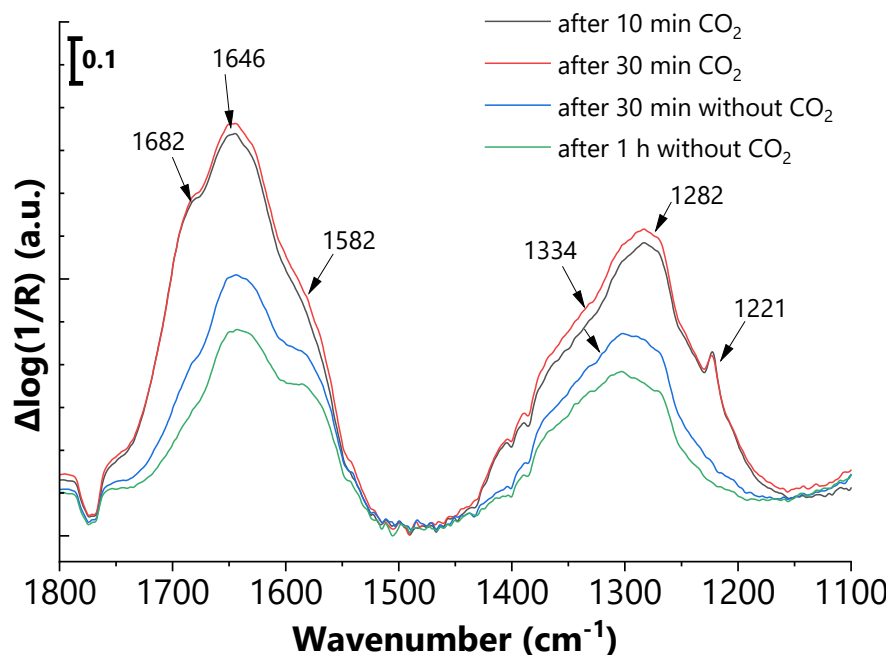
Figure S23. CO_2 adsorption over STO-SCO (HT).
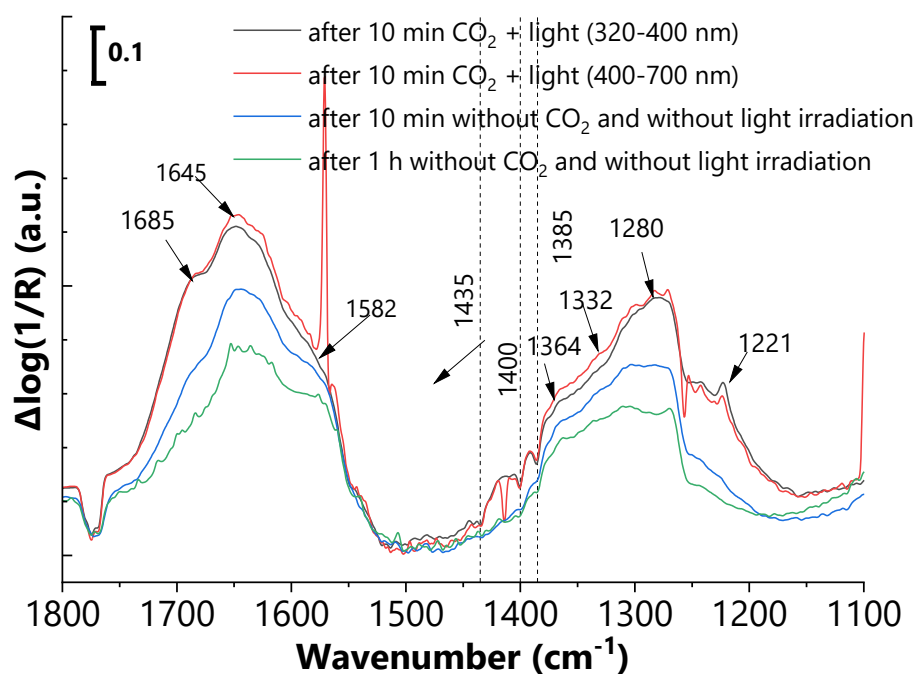

Figure S24. CO_2 adsorption over STO-SCO (HT) under irradiation.
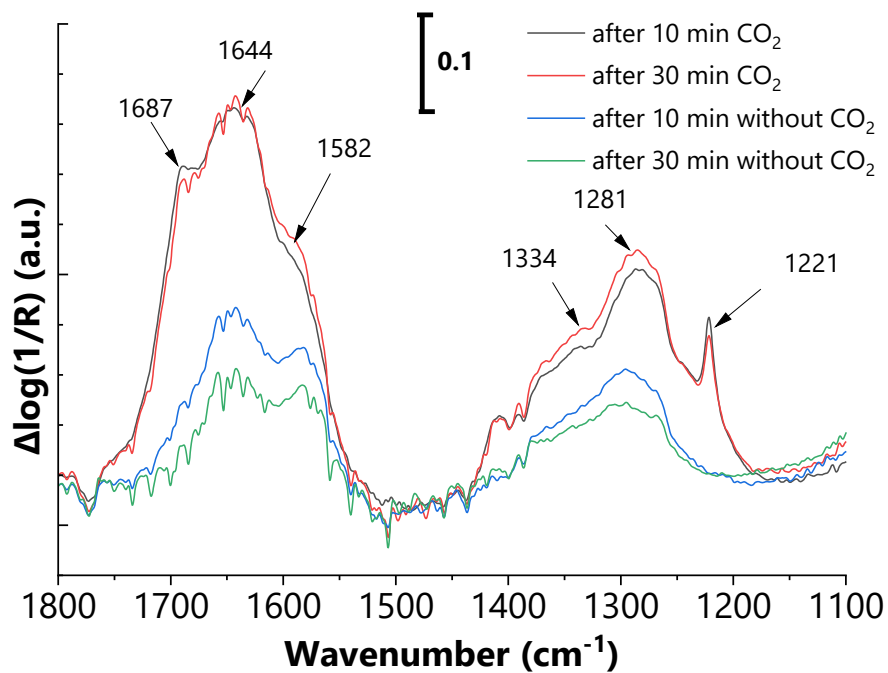
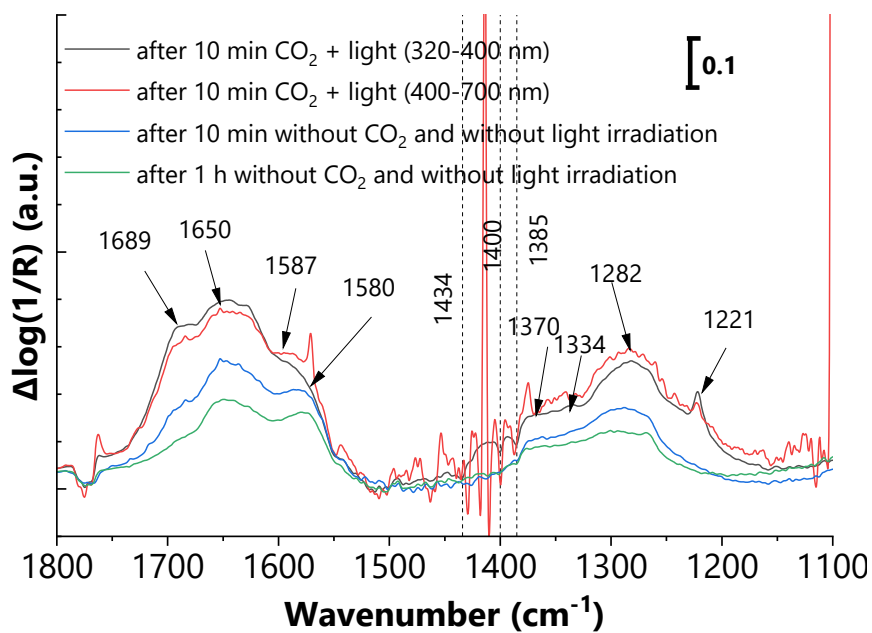**Figure S25**. CO_2 adsorption over NiO/STO-SCO (HT).

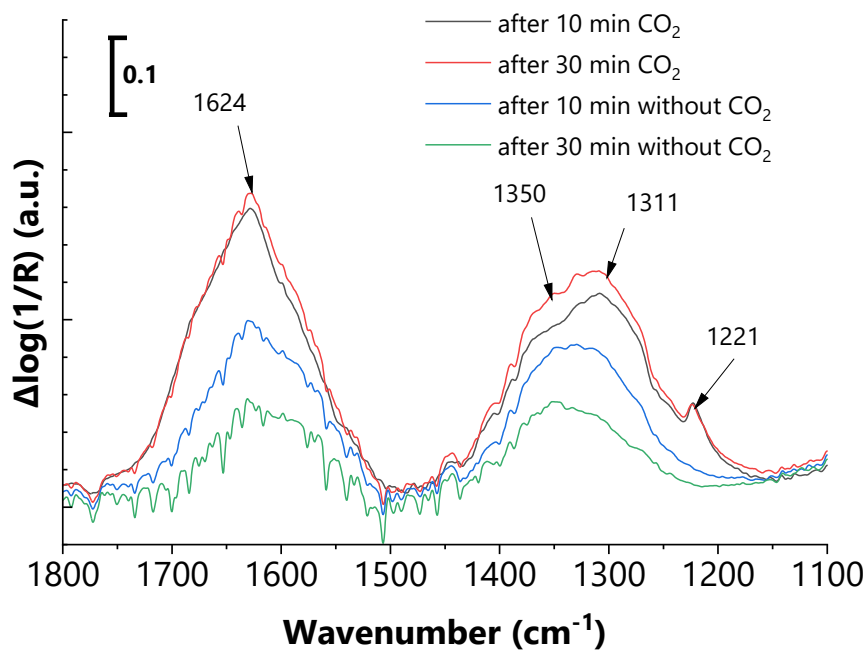**Figure S26**. CO_2 adsorption over NiO/STO-SCO (HT) under irradiation.

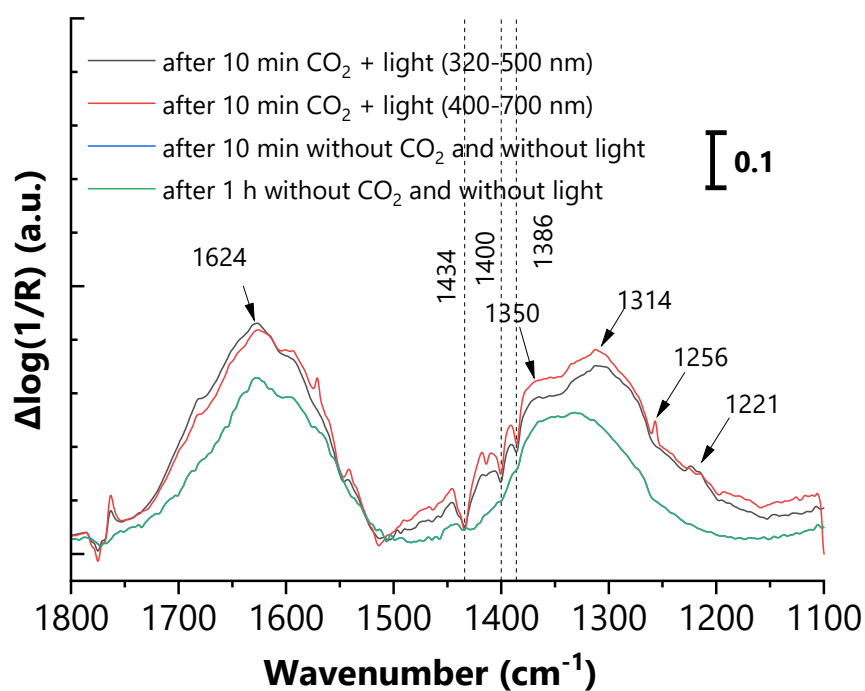**Figure S27**. CO_2 adsorption over Au-STO-SCO (HT).

Figure S28. CO_2 adsorption over Au-STO-SCO (HT) under irradiation.

Table S7. Systematic approach for the assignment of vibrational bands during CO_2 adsorption over Au-NiO/STO-SCO (HT).

Species	In the dark	Under irradiation	
		λ: 320-500 nm	λ: 500-700 nm
Linearly adsorbed CO_2	1270	1270	1270
Monodentate bicarbonates	1221 +1624 [10]	1221 +1375+1624	Disappeared, visible light induced transformation of monodentate bicarbonates
Bidentate carbonate	1586	1560+1309	1560 +1414
Carboxylates	1350+1624 [9]	--	--
Spectator carbonate species	---	1550, 1515,1435, 1400,1390	1550, 1515,1435, 1400,1390

Table S8. Systematic approach for the assignment of vibrational bands under irradiation 320-500 nm

Species	Au-NiO/STO-SCO (HT)	Au-STO-SCO (HT)	NiO/STO-SCO (HT)	STO-SCO (HT)
Linearly adsorbed CO_2	--	--	1282	1280
Monodentate carbonate	--	---	1582 [10]	1582 cm-1 [10]
Monodentate bicarbonates	1221+1624 +1375 [10]	1221 +1624 [10]	1221 +1689 +1370[10]	
Bidentate bicarbonate	--	--	1221 +1689 [10]	1221 +1685 [10]
Bidentate carbonate	1309+1560 [10]	1314 [10]	--	1364 [19]
Carboxylates		1350+1624 [9]	1334+1650 [9]	1332+1645
Spectator carbonate species	1550, 1515,1435, 1400,1390	--	--	--

Table S9. Systematic approach for the assignment of vibrational bands under irradiation from the visible range (500-700 nm)

Species	Au-NiO/STO-SCO (HT)	Au-STO-SCO (HT)	NiO/STO-SCO (HT)	STO-SCO (HT)
Linearly adsorbed CO_2	1270	--	1282	1280
Monodentate carbonate		---	1580 [10]	1582 [10]
Monodentate bicarbonates	Disappeared, visible-light induced transformation of monodentate bicarbonates	1221 +1624 [10]	1221 +1687 +1370 [10]	1221 +1685 [10]
Bidentate bicarbonate	--	--	1221 +1689 +1370 [10]	1221 +1685 [10]
Bidentate carbonate	1560+1414	1314 [10]	--	1364 [19]
Carboxylates	--	1350+1624 +1256 [9]	1334 +1650 [9]	1332+1645
Spectator carbonate species	1550, 1515,1435, 1400,1390			

Section 10: CO₂ reduction experiments
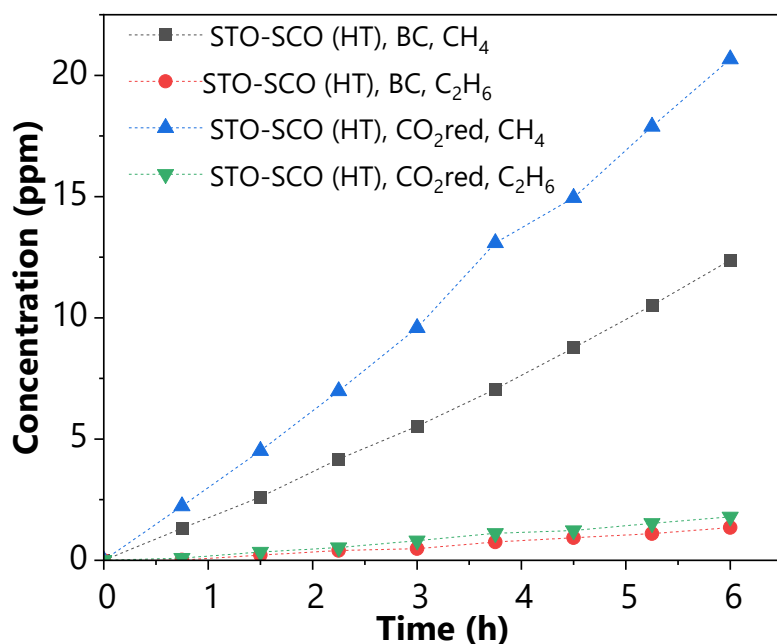
Figure S29: Concentration of CH_4 and C_2H_6 formed over STO-SCO (HT) during batch cleaning (BC) and CO_2 reduction (CO₂red).
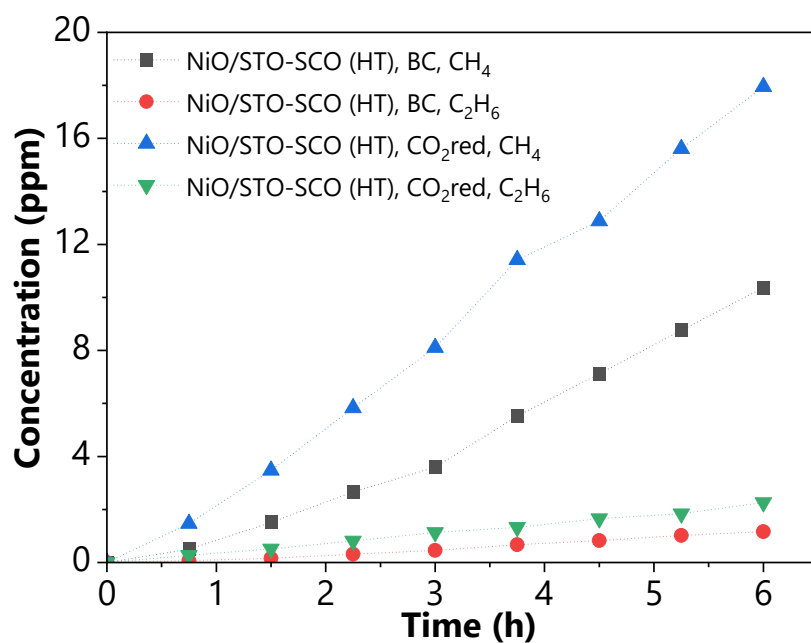
Figure S30. Concentration of CH_4 and C_2H_6 formed over NiO/STO-SCO (HT) during batch cleaning (BC) and CO_2 reduction (CO₂red).
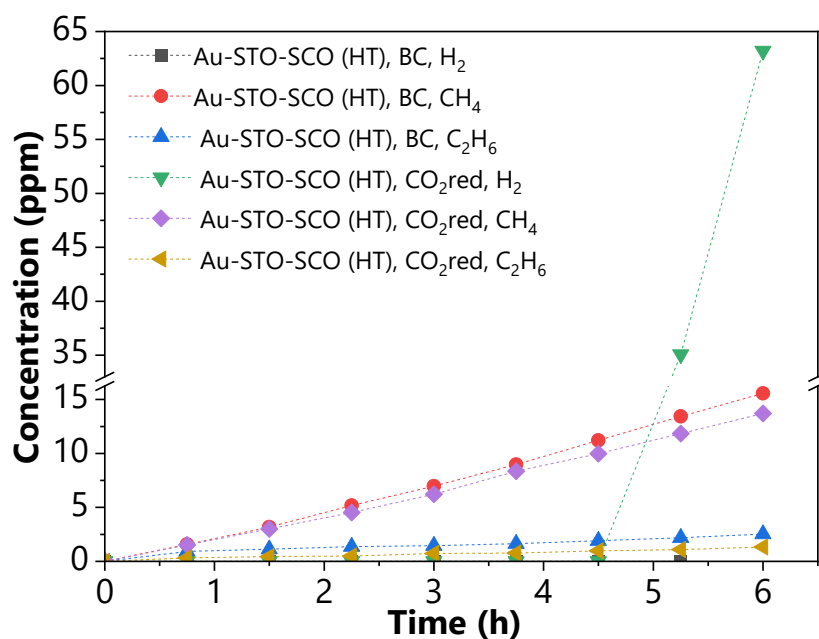
Figure S31. Concentration of CH_4, C_2H_6 and H_2 formed over Au-STO-SCO (HT) during batch cleaning (BC) and CO_2 reduction (CO_2red).
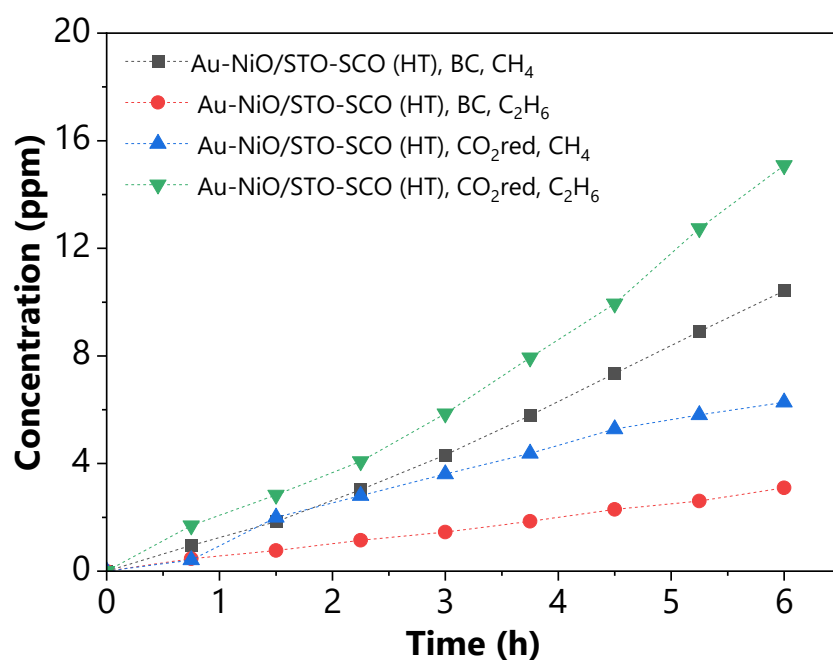
Figure S32. Concentration of CH_4, C_2H_6 and H_2 formed over Au-NiO/STO-SCO (HT) during batch cleaning (BC) and CO_2 reduction (CO_2red).
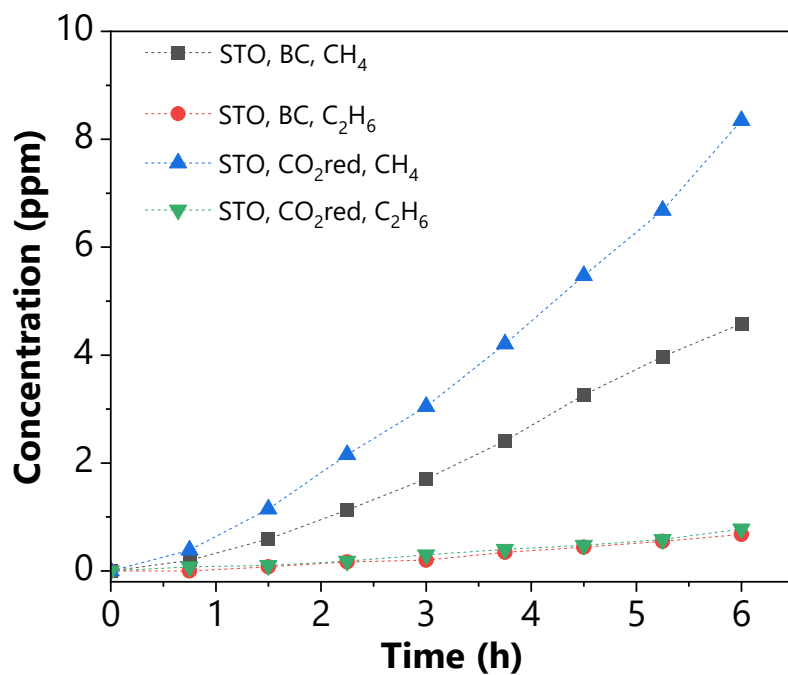
Figure S33. Concentration of CH_4 and C_2H_6 formed over STO during batch cleaning (BC) and CO_2 reduction (CO_2red).

Figure S34. Concentration of CH_4 and C_2H_6 formed over NiO/STO during batch cleaning (BC) and CO2 reduction (CO_2red).

Figure S35. Concentration of CH_4 and C_2H_6 formed over Au-STO during batch cleaning (BC) and CO_2 reduction (CO_2red).
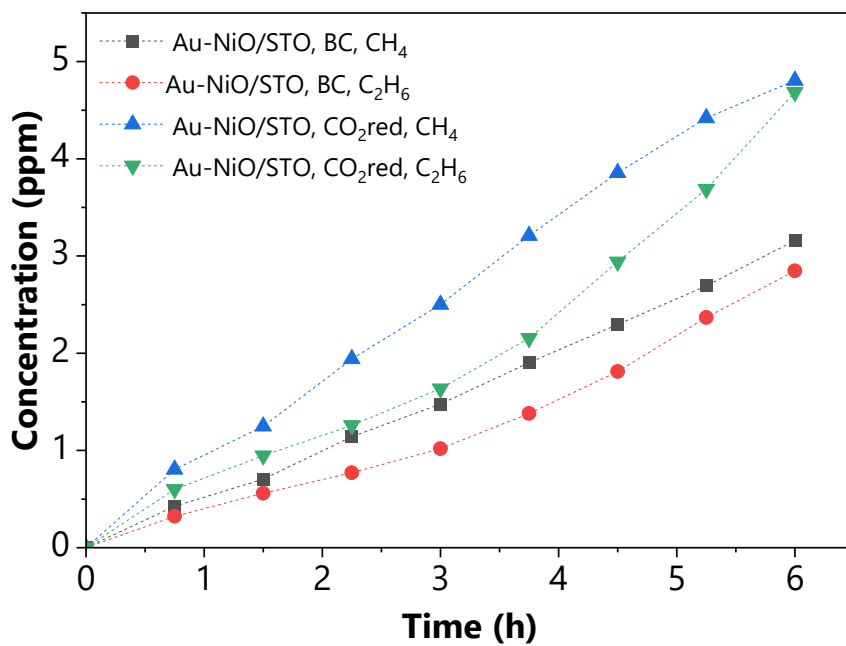
Figure S36. Concentration of CH_4 and C_2H_6 formed over Au-NiO/STO during batch cleaning (BC) and CO_2 reduction (CO_2red).
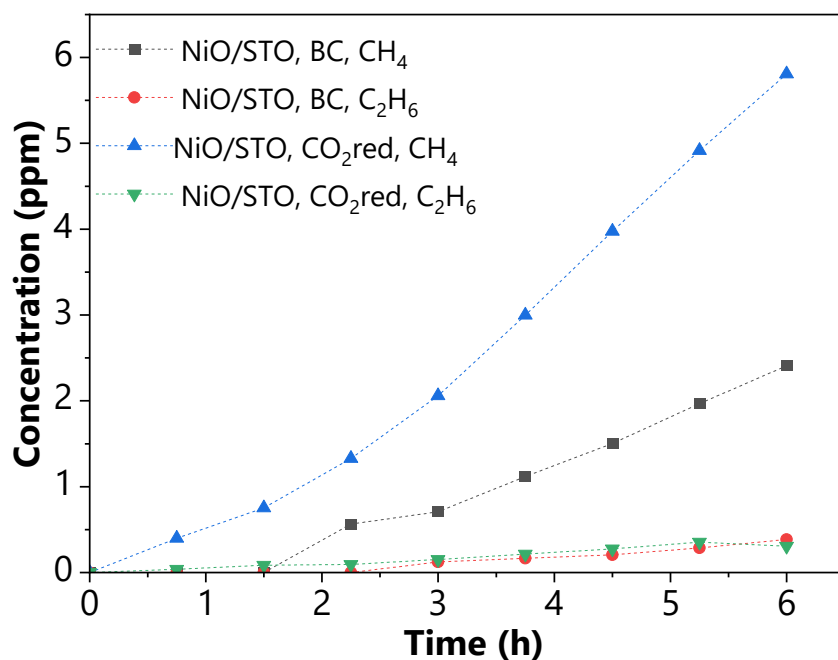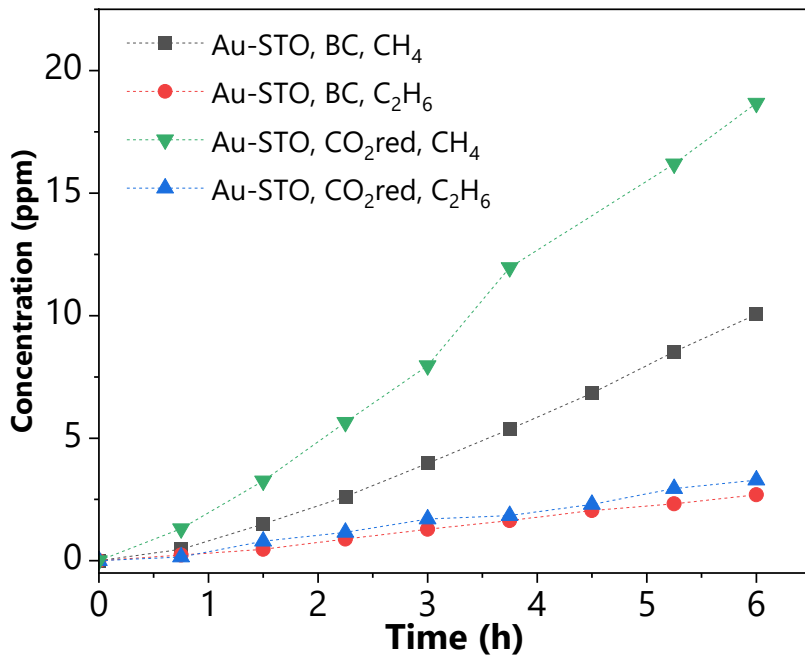
Section 11: The determination of the conduction and valence band edges of the components

Component 1. STO

The Mott-Schottky measurement of STO was performed using a Zennium three-electrode setup (Zahner, Germany). The reference electrode was Ag/AgCl (3 M NaCl), the counter electrode was a Pt wire. The working electrode was prepared by the well-known coating method. First, the mixture of 20 mg catalyst, 900 μl isopropanol and 100 μL nafion was undertaken ultrasonication for 10 minutes. Second, the as prepared dispersion was dropped and dried on a conductive glass (FTO, with an active surface 1.5x1.5 cm^2). The electrolyte was 0.5 M aqueous solution of Na$_2$SO$_4$.

Figure S37. Mott-Schottky plot of STO.

The flat band potential of SrTiO$_3$ was experimental determined from Mott-Schottky plot (E_{FB} = -1.21 V vs Ag/AgCl at pH=7). To calculate the potential value against the normal hydrogen electrode (NHE), Equation (1) was used with $E^0_{Ag/AgCl} = 0.21$ V [20, 21]

$$E_{FB(STO)} = E_{Ag/AgCl} + E^0_{Ag/AgCl} \qquad = \text{-1.21} + 0.21 = \text{-1.00 V vs NHE (pH=7)} \qquad (1)$$

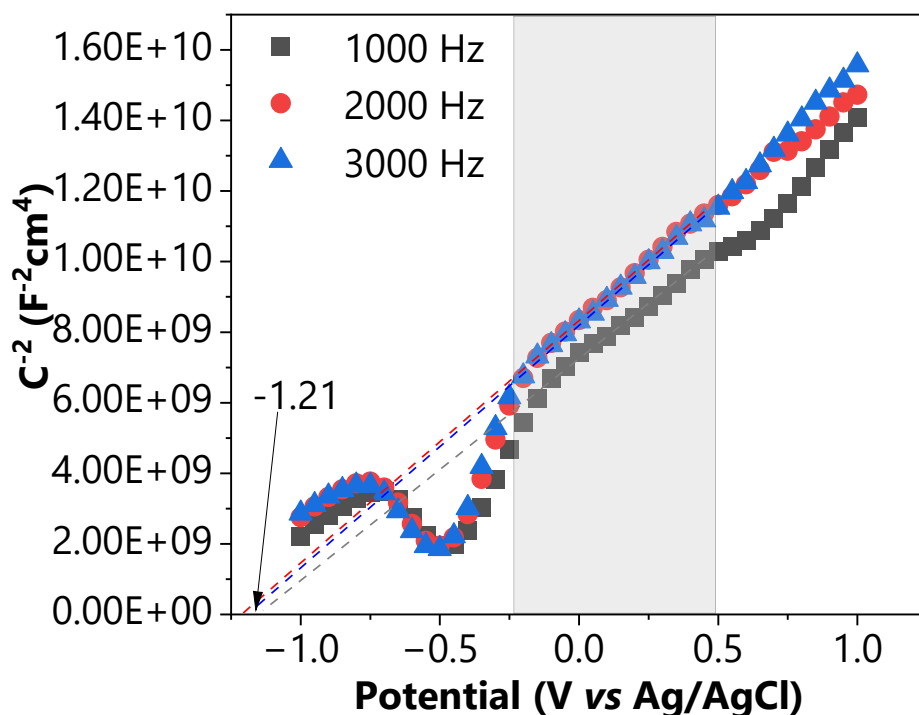The experimentally determined flatband potential for STO is in concordance with the values reported by Wang and coworkers [22].

Furthermore, the CB edge of SrTiO$_3$ is then calculated as given in Equation (2):

$$E_{CB,STO} = E_{FB,STO} - 0.1 = -1.10 \text{ V vs NHE (pH} = 7) \tag{2}$$

The VB edge of STO is then calculated by Equation (3) with $\Delta E_g = 3.2$ eV.

$$E_{VB,STO} = E_{VB,STO} + \Delta E_g, = -1.10 + 3.2 = 2.1 \text{ V vs NHE (pH} = 7) \tag{3}$$

Component 2. NiO

The flatband position of NiO was reported in the literature, and it is equal to 0.30 V vs NHE at pH = 7 [22]. Furthermore, the experimentally determined value for the valence band edge of NiO was 0.37 V vs. NHE at pH=7[23]. Considering the band gap value of NiO from the literature (i.e., 3.4 eV [24]), it can be concluded that the position of CB edge of NiO is located at -3.03 V *vs.* NHE at pH = 7.

Component 3. SCO

The CB and VB edges of SrCO$_3$ were taken from the values reported in the literature based on experimental findings [25].

$E_{CB,SrCO3} = $ -0.97 V vs SCE

$E_{VB, SrCO3} = 3.93$ V vs SCE

To calculate the potential value against the normal hydrogen electrode, Equation (1) was applied.

$E^0_{Hg/Hg_2Cl_2} = 0.334$ V in 0.1 M KCl [20, 21]

$E_{CB,SrCO3} = -0.97 + 0.334 = -0.636$ V vs NHE (pH = 7)

$E_{VB,SrCO3} = 3.93 + 0.334 = 4.264$ V vs NHE (pH = 7)

With this information the VB and CB edge positions of the materials before contacting them are plotted in Figure S38.

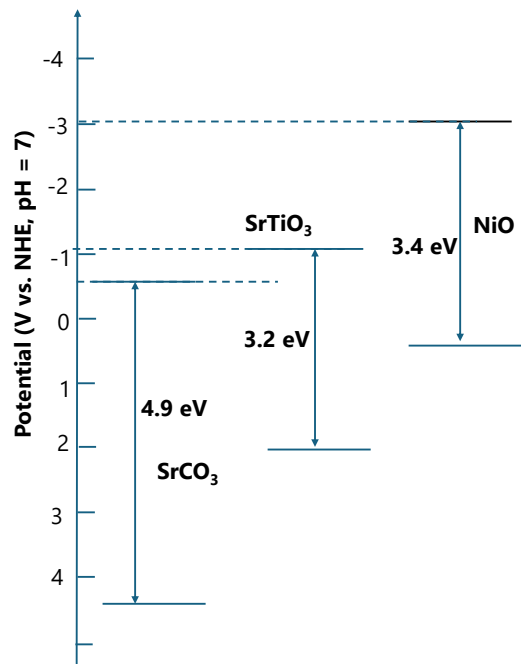**Figure S38.** Overview of the band edge positions of the components.
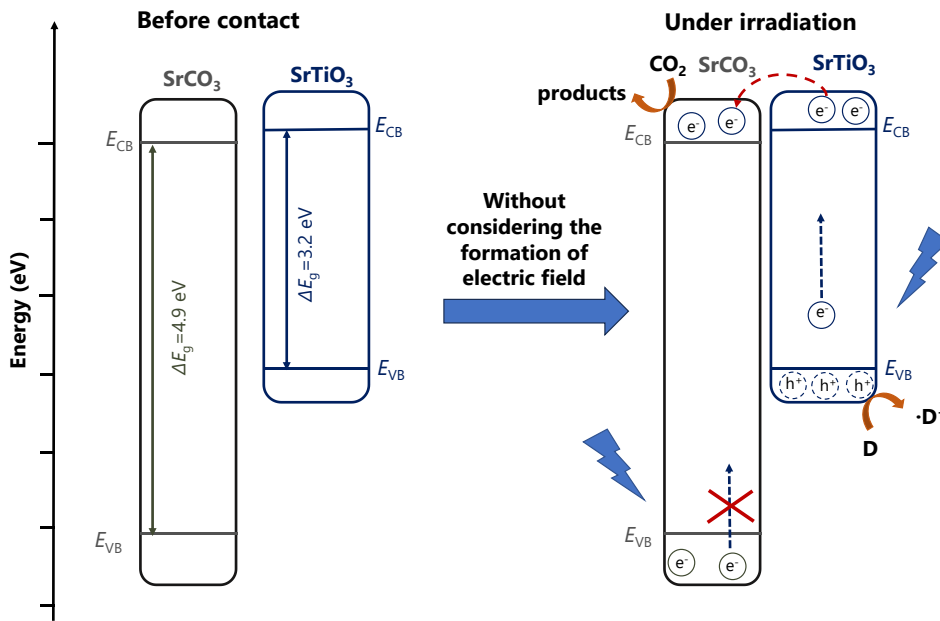
Section 12: Charge transfer mechanisms

Figure S39. Scheme of charge transfer in case of SrTiO$_3$-SrCO$_3$ by neglecting the formation of internal electric field [25, 26].
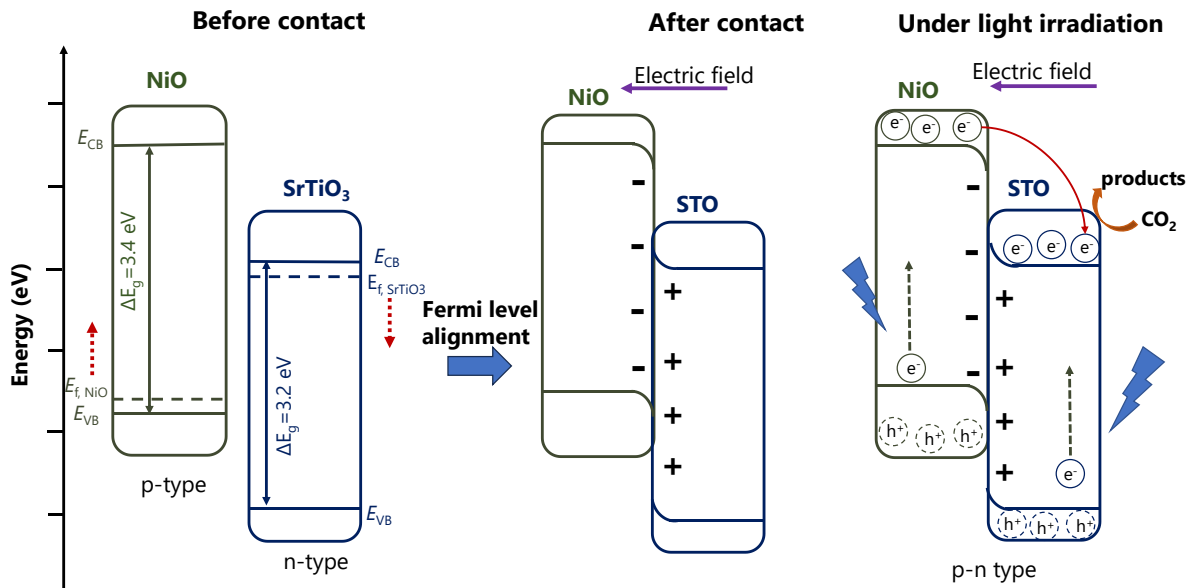

Figure S40. Charge transfer mechanism in case of NiO/SrTiO$_3$ (The electronic data was taken from [27]).
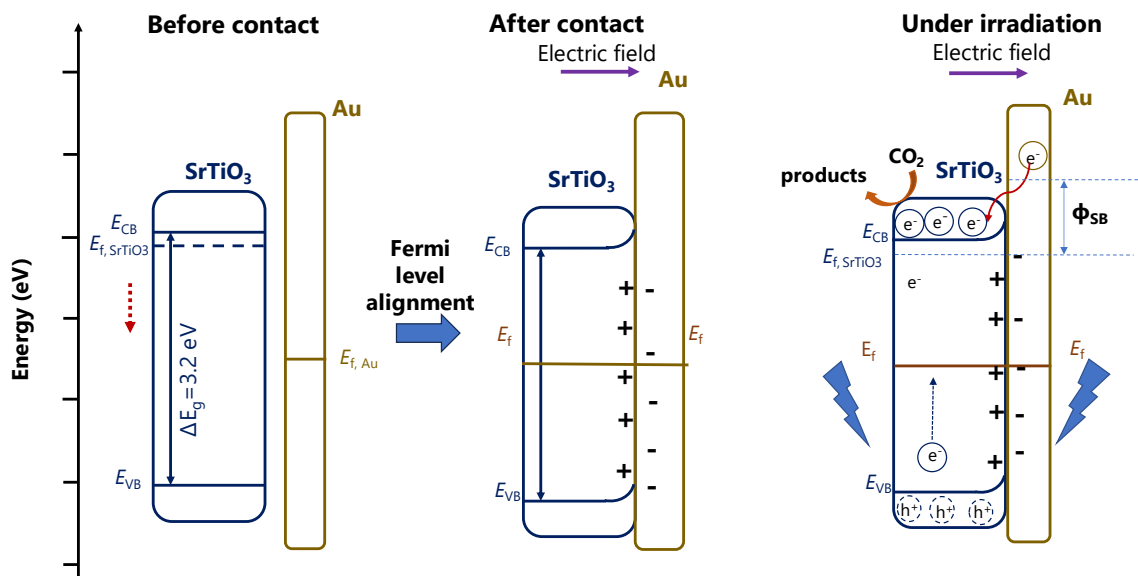
Figure S41. The charge transfer in case of Au-SrTiO$_3$ [28].

Section 13: DFT calculations

Density states of bulk SrTiO₃ and SrCO₃

At first, density of states of bulk SrTiO₃ and SrCO₃ are calculated and compared with references [29, 30]. The band gap of bulk SrTiO₃ calculated with DFT method is 1.78 eV (Fig. S42), which is much underestimated compared with experiment value (3.75 eV [29]). To overcome this problem, the Hubbard interaction corrected DFT+U formalism was used. Based on Ahmed's work [28], DFT+U method with U = 14.5 eV in Ti-3d orbital resulted in band gap of 3.72 eV for SrTiO₃, which is closely matched with the experimental value. Thus, all calculations including Ti used U = 14.5 eV to obtain reasonable results. The density of states of orthorhombic SrCO₃ bulk are shown in Fig. S43. The DFT calculated band gap of 4.42 eV is consistent with the reference value (4.45 eV) [30].
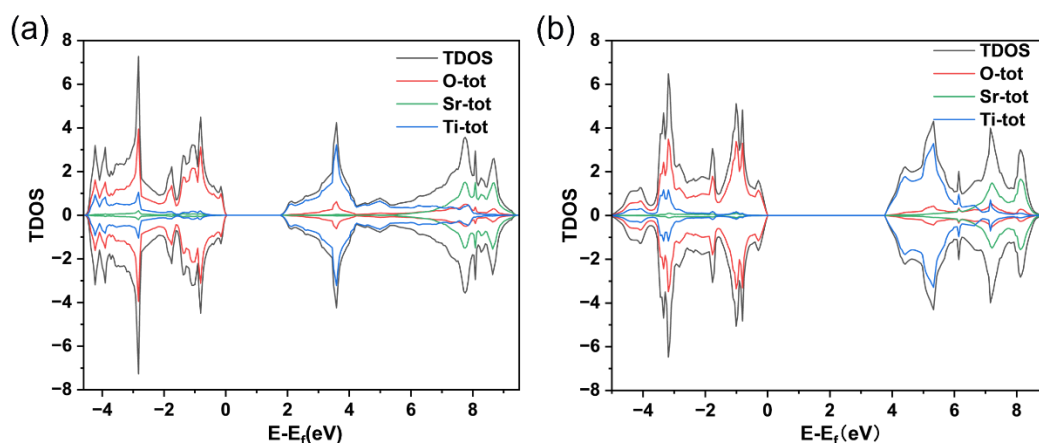
Figure S42. Total density of states (TDOS) and its projection onto O, Sr and Ti atoms of cubic SrTiO₃ bulk; (a) using DFT; and (b) using DFT+U method.
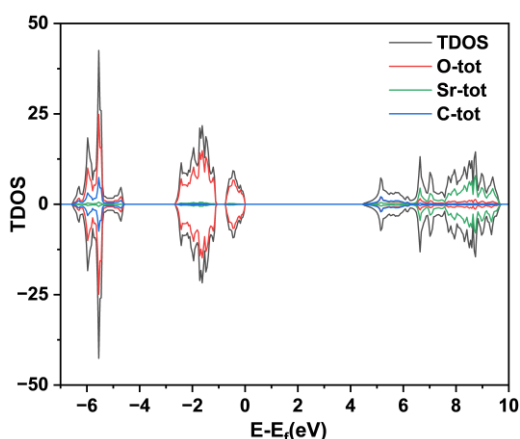
Figure S43. Total density of states (TDOS) and its projection onto O, Sr, and C atoms of orthorhombic SrCO₃ bulk using DFT.

Model and TDOS of SrO-terminated STO (110) and C-doped SrO-terminated STO
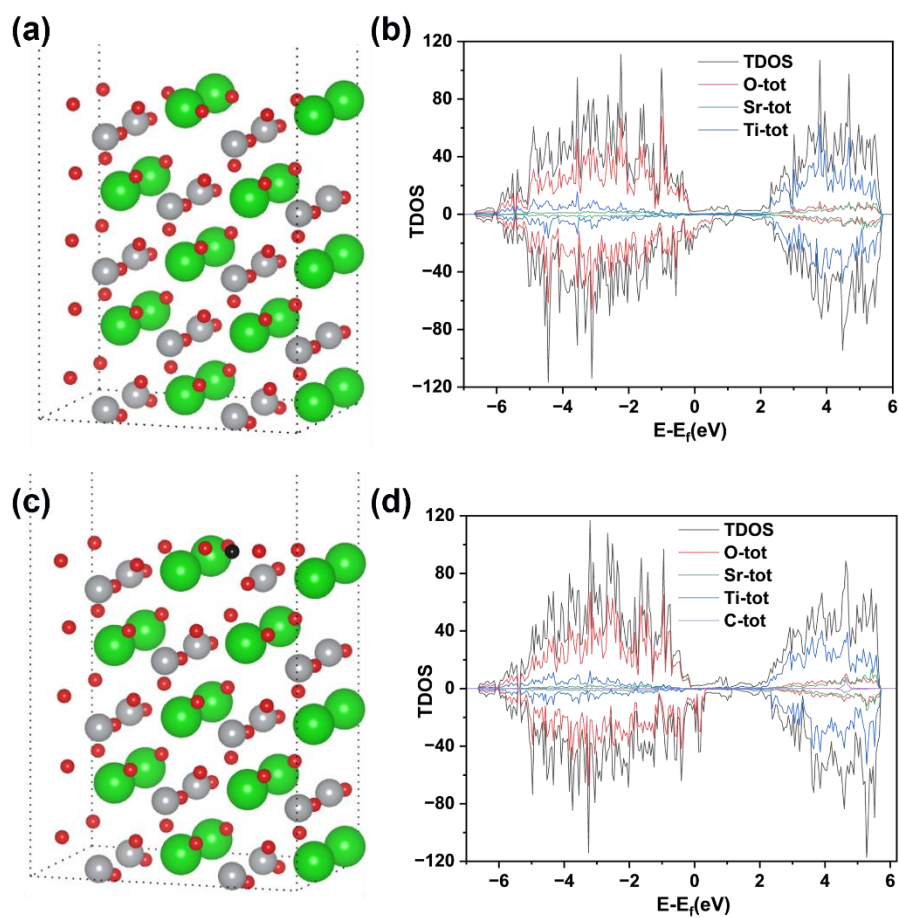
Figure S44. Model of SrO-terminated SrTiO$_3$(110) (a) and TDOS (b); Model of C doped SrO-terminated SrTiO$_3$(111) (c) and TDOS (d).

Model and TDOS of TiO-terminated SrTiO₃ (110) and C-doped TiO-terminated SrTiO₃
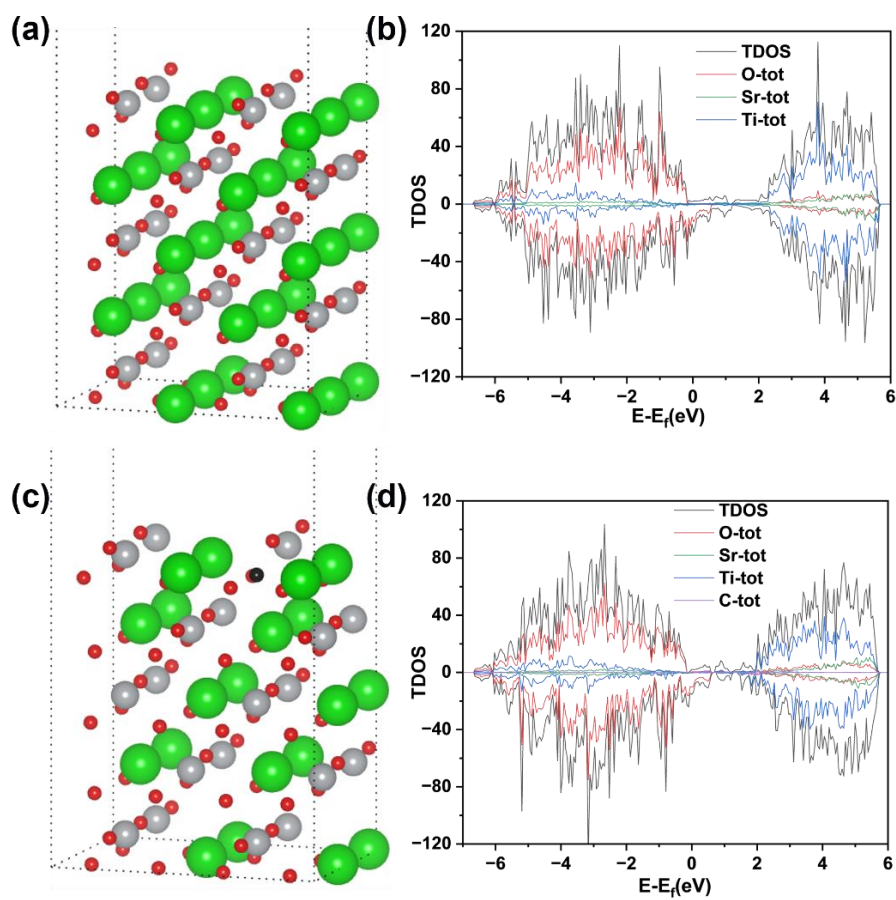
Fig.S45. Model of TiO-terminated SrTiO₃(110) (a) and TDOS (b); C doped TiO-terminated SrTiO₃(111) (c) and TDOS (d).

Model and TDOS of SrCO₃ (111) and C-doped SrCO₃
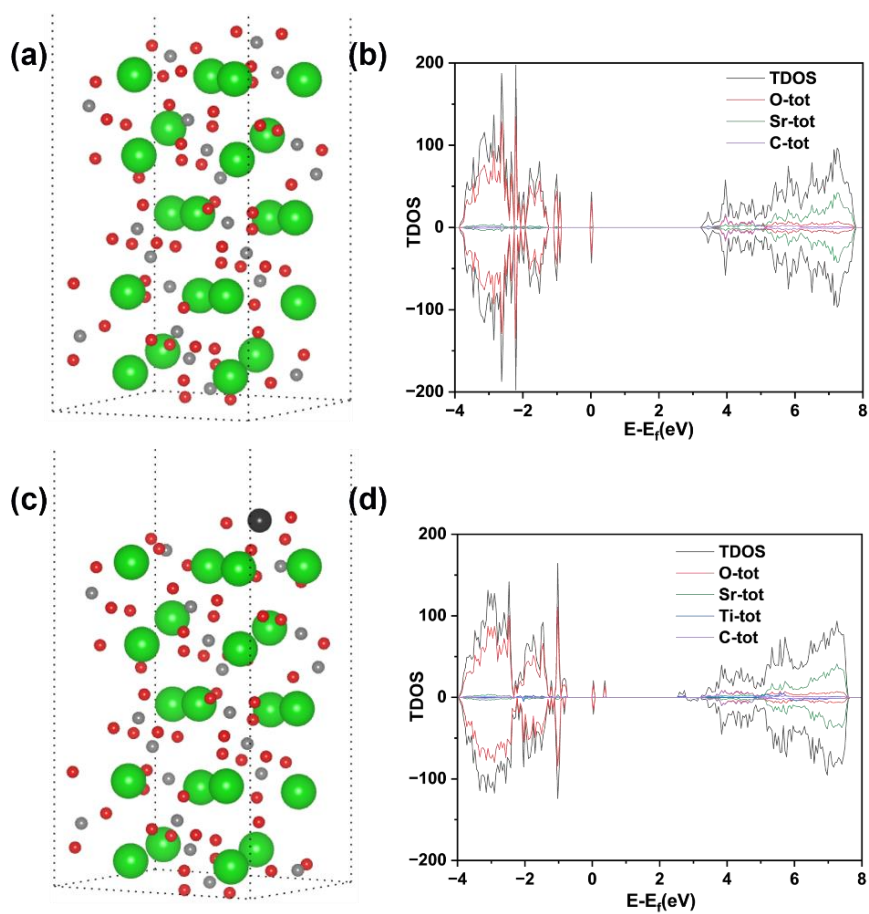
Figure S46. Model of SrCO₃ (111) (a) and TDOS (b); model of C doped SrCO₃(111) (c) and TDOS (d).

References

(1) Gerhold, S.; Riva, M.; Wang, Z.; Bliem, R.; Wagner, M.; Osiecki, J.; Schulte, K.; Schmid, M.; Diebold, U. Nickel-oxide-modified SrTiO$_3$ (110)-(4× 1) surfaces and their interaction with water. *The Journal of Physical Chemistry C* **2015**, *119* (35), 20481-20487.

(2) Sønsteby, H. H.; Skaar, E.; Fjellvåg, Ø. S.; Bratvold, J. E.; Fjellvåg, H.; Nilsen, O. A foundation for complex oxide electronics-low temperature perovskite epitaxy. *Nature communications* **2020**, *11* (1), 2872.

(3) Chang, W. T.; Sharma, S.; Liao, J. H.; Kahlal, S.; Liu, Y. C.; Chiang, M. H.; Saillard, J. Y.; Liu, C. Heteroatom-Doping Increases Cluster Nuclearity: From an [Ag$_{20}$] to an [Au$_3$Ag$_{18}$] Core. *Chemistry–A European Journal* **2018**, *24* (54), 14352-14357.

(4) Cai, S.; Chen, J.; Li, Q.; Jia, H. Enhanced photocatalytic CO$_2$ reduction with photothermal effect by cooperative effect of oxygen vacancy and Au cocatalyst. *ACS Applied Materials & Interfaces* **2021**, *13* (12), 14221-14229.

(5) Priebe, J. B.; Karnahl, M.; Junge, H.; Beller, M.; Hollmann, D.; Brückner, A. Water reduction with visible light: synergy between optical transitions and electron transfer in Au-TiO$_2$ catalysts visualized by in situ EPR spectroscopy. *Angewandte Chemie International Edition* **2013**, *52* (43), 11420-11424.

(6) Han, S.; Yu, L.; Zhang, H.; Chu, Z.; Chen, X.; Xi, H.; Long, J. Gold plasmon-enhanced solar hydrogen production over SrTiO$_3$/TiO$_2$ heterostructures. *ChemCatChem* **2019**, *11* (24), 6203-6207.

(7) Zhang, Z.; Wang, X.; Long, J.; Gu, Q.; Ding, Z.; Fu, X. Nitrogen-doped titanium dioxide visible light photocatalyst: spectroscopic identification of photoactive centers. *Journal of Catalysis* **2010**, *276* (2), 201-214.

(8) Okumura, M.; Coronado, J. M.; Soria, J.; Haruta, M.; Conesa, J. C. EPR study of CO and O$_2$ interaction with supported Au catalysts. *Journal of Catalysis* **2001**, *203* (1), 168-174.

(9) Bando, K. K.; Sayama, K.; Kusama, H.; Okabe, K.; Arakawa, H. In-situ FT-IR study on CO$_2$ hydrogenation over Cu catalysts supported on SiO$_2$, Al$_2$O$_3$, and TiO2. *Applied Catalysis A: General* **1997**, *165* (1-2), 391-409.

(10) Mino, L.; Spoto, G.; Ferrari, A. M. CO$_2$ capture by TiO$_2$ anatase surfaces: a combined DFT and FTIR study. *The Journal of Physical Chemistry C* **2014**, *118* (43), 25016-25026.

(11) Baltrusaitis, J.; Schuttlefield, J.; Zeitler, E.; Grassian, V. H. Carbon dioxide adsorption on oxide nanoparticle surfaces. *Chemical Engineering Journal* **2011**, *170* (2-3), 471-481.

(12) Wu, W.; Bhattacharyya, K.; Gray, K.; Weitz, E. Photoinduced reactions of surface-bound species on titania nanotubes and platinized titania nanotubes: an in situ FTIR study. *The Journal of Physical Chemistry C* **2013**, *117* (40), 20643-20655.

(13) Bhattacharyya, K.; Danon, A.; K. Vijayan, B.; Gray, K. A.; Stair, P. C.; Weitz, E. Role of the surface lewis acid and base sites in the adsorption of CO_2 on titania nanotubes and platinized titania nanotubes: an in situ FT-IR study. *The Journal of Physical Chemistry C* **2013**, *117* (24), 12661-12678.

(14) Martra, G. Lewis acid and base sites at the surface of microcrystalline TiO_2 anatase: relationships between surface morphology and chemical behaviour. *Applied Catalysis A: General* **2000**, *200* (1-2), 275-285.

(15) Su, W.; Zhang, J.; Feng, Z.; Chen, T.; Ying, P.; Li, C. Surface phases of TiO_2 nanoparticles studied by UV Raman spectroscopy and FT-IR spectroscopy. *The Journal of Physical Chemistry C* **2008**, *112* (20), 7710-7716.

(16) Liao, L.-F.; Lien, C.-F.; Shieh, D.-L.; Chen, M.-T.; Lin, J.-L. FTIR study of adsorption and photoassisted oxygen isotopic exchange of carbon monoxide, carbon dioxide, carbonate, and formate on TiO_2. *The Journal of Physical Chemistry B* **2002**, *106* (43), 11240-11245.

(17) Rasko, J.; Solymosi, F. Infrared spectroscopic study of the photoinduced activation of CO_2 on TiO_2 and Rh/TiO_2 catalysts. *The Journal of Physical Chemistry* **1994**, *98* (29), 7147-7152.

(18) Bernitt, D.; Hartman, K.; Hisatsune, I. Infrared spectra of isotopic bicarbonate monomer ions. *The Journal of Chemical Physics* **1965**, *42* (10), 3553-3558.

(19) Yang, C.-C.; Yu, Y.-H.; van der Linden, B.; Wu, J. C.; Mul, G. Artificial photosynthesis over crystalline TiO_2-based catalysts: fact or fiction? *Journal of the American Chemical Society* **2010**, *132* (24), 8398-8406.

(20) Bui, D.-P.; Pham, M.-T.; Tran, H.-H.; Nguyen, T.-D.; Cao, T. M.; Pham, V. V. Revisiting the key optical and electrical characteristics in reporting the photocatalysis of semiconductors. *ACS omega* **2021**, *6* (41), 27379-27386.

(21) Meites, L. Handbook of analytical chemistry. *Soil Science* **1963**, *96* (5), 358.

(22) Wang, L.; Wang, Z.; Wang, D.; Shi, X.; Song, H.; Gao, X. The photocatalysis and mechanism of new $SrTiO_3/TiO_2$. *Solid state sciences* **2014**, *31*, 85-90.

(23) Natu, G.; Hasin, P.; Huang, Z.; Ji, Z.; He, M.; Wu, Y. Valence band-edge engineering of nickel oxide nanoparticles via cobalt doping for application in p-type dye-sensitized solar cells. *ACS applied materials & interfaces* **2012**, *4* (11), 5922-5929.

(24) Uddin, M. T.; Nicolas, Y.; Olivier, C.; Jaegermann, W.; Rockstroh, N.; Junge, H.; Toupance, T. Band alignment investigations of heterostructure NiO/TiO_2 nanomaterials used as

efficient heterojunction earth-abundant metal oxide photocatalysts for hydrogen production. *Physical Chemistry Chemical Physics* **2017**, *19* (29), 19279-19288.

(25) Jin, S.; Dong, G.; Luo, J.; Ma, F.; Wang, C. Improved photocatalytic NO removal activity of $SrTiO_3$ by using $SrCO_3$ as a new co-catalyst. *Applied Catalysis B: Environmental* **2018**, *227*, 24-34.

(26) Li, Z.; Zheng, P.; Zhang, W.; Gong, S.; Zhu, L.; Xu, J.; Rao, F.; Xie, X.; Zhu, G. Constructing $SrCO_3$/$SrTiO_3$ nanocomposites with highly selective photocatalytic CO_2-to-CO reduction. *Colloids and Surfaces A: Physicochemical and Engineering Aspects* **2022**, 129686.

(27) Zhang, K. H.; Wu, R.; Tang, F.; Li, W.; Oropeza, F. E.; Qiao, L.; Lazarov, V. K.; Du, Y.; Payne, D. J.; MacManus-Driscoll, J. L. Electronic structure and band alignment at the NiO and $SrTiO_3$ p–n heterojunctions. *ACS applied materials & interfaces* **2017**, *9* (31), 26549-26555.

(28) Guo, W.; Huang, J.; Wei, W. D. Plasmonic Metal/Semiconductor Heterostructures. In *Plasmonic Catalysis: From Fundamentals to Applications* (Eds. Camargo, H.C.P. & Cortés, E.)*, Wiley-VCH,* Weinheim, Germany, **2021**, 295-322.

(29) Ahmed, S.; Hasan, T.; Faysal, A. K. M. S. H.; Nishat, S. S.; Khan, M. N. I.; Kabir, A.; Ahmed, I. A DFT+U approach to doped $SrTiO_3$ for solar harvesting applications. *Computational Materials Science* **2022**, *214*, 111743.

(30) Hu, Z.; Li, Y.; Zhang, C.; Ao, B. Structural, electronic, optical and bonding properties of strontianite, $SrCO_3$: First-principles calculations. *Journal of Physics and Chemistry of Solids* **2016**, *98*, 65-70.